Chronology and eccentricity phasing for the Early Turonian greenhouse (~93-94 Ma): constraints on astronomical control of the carbon cycle

Jiří Laurin[1], David Uličný[1], Stanislav Čech[2], Jakub Trubač[3], Jiří Zachariáš[3], Andrea Svobodová[4]

[1] *Institute of Geophysics of the Czech Academy of Sciences, Boční II/1401, 141 31 Prague, Czech Republic*

[2] *Czech Geological Survey, Prague, Czech Republic*

[3] *Institute of Geochemistry, Mineralogy and Mineral Resources, Charles University, Prague, Czech Republic*

[4] *Institute of Geology of the Czech Academy of Sciences, Prague, Czech Republic*

ABSTRACT

The Early Turonian interval represents a unique confluence of climatic and oceanographic conditions including peak surface temperatures, high greenhouse-gas concentrations and maximum Phanerozoic sea level. The susceptibility of this climate mode to astronomical insolation forcing remains poorly understood partly due to a limited time control and unknown phasing of astronomical cycles in this interval. Here we offer a refined astrochronology of the Early Turonian based on laterally consistent precession signals preserved in offshore strata of the Bohemian Cretaceous Basin (central Europe). Pristine amplitude modulation verified through interference patterns in depth-frequency plots provides a robust indication of ~100-kyr and 405-kyr eccentricity phases (maxima and minima) that are pinned to ammonite biozones and new carbon-

isotope data from two cores. The Early Turonian is estimated as 885 ±41 (2σ) thousand years (kyr) in duration, with the Cenomanian/Turonian boundary predating the first Turonian 405-kyr maximum (no. 232 in the Geological Time Scale 2020) by 82 ±70 (2σ) kyr. The results support a possible link of the recovery from Oceanic Anoxic Event II to increasing magnitude of seasonal insolation extremes due to rising eccentricity on 405-kyr and million-year (Myr) time scales. Superimposed upon this trend are small-scale carbon-isotope anomalies the pacing of which passes from ~110 kyr, resembling short eccentricity, to ~170-kyr, possibly related to obliquity modulation. This eccentricity-to-obliquity transition paralleling the rising phase of Myr-scale eccentricity cycle suggests decoupling of the carbon-cycle perturbations from low-latitude seasonal insolation and involvement of mid- to high-latitude carbon reservoirs.

1. INTRODUCTION

Following a major climatic perturbation related to the Oceanic Anoxic Event II (OAE II; Schlanger and Jenkyns, 1976), the Early Turonian, ~93-94 million years (Myr) ago, was an episode of stabilized climate of what is considered the peak Phanerozoic greenhouse warmth (Clarke and Jenkyns 1999; Friedrich et al. 2012). Both surface temperatures and global sea level reached extreme levels owing primarily to high rates of ocean-crust production and CO_2 outgassing (e.g., Jones and Jenkyns 2001). Compared to OAE II, the carbon-isotope ratios in marine carbonates and organic matter are enriched in the isotope ^{12}C suggesting reduced capacity of oceanic and terrestrial organic reservoirs, i.e., improved recycling of organic carbon that likely contributed to radiative forcing. Short-term (10^4-year scale) carbon-isotope anomalies with magnitudes 0.2-0.5 ‰ in both organic and carbonate carbon (Jarvis et al. 2006, 2015; Fig. 1) point to transient perturbations to the carbon cycle of possible Milankovitch origin (Voigt et al. 2007). The Early Turonian thus represents an example of peak greenhouse climate, destabilized on short time scales by external forcings. The potential astronomical origin represents a testable hypothesis that can be evaluated with detailed temporal constraints.

Earlier astrochronologies suggested durations of the Early Turonian in the range of 0.78 to 0.84 Myr (Sageman et al. 2006; Voigt et al. 2008; Tab. 1), but a substantial (~20%) disagreement exists between these estimates and the duration provided by the Geological Time Scales (GTS 2012, Ogg and Hinnov 2012; GTS 2020, Gale et al. 2020). More recent studies (Sprovieri et al. 2013; Eldrett et al. 2015; Batenburg et al. 2016) provided detailed astronomical

63 contexts including the phases of orbital eccentricity, but their
64 chronostratigraphy remains partly controversial (Fig. 1; Tab. 1).
65 In order to test the published results and contribute further details on the
66 temporal framework, we present a new astrochronology based on well-
67 preserved precessional and eccentricity signals in the Bohemian Cretaceous
68 Basin. The results offer a robust interpretation of ~100-kyr, 405-kyr and ~2.4-
69 Myr eccentricity phases that provide new insights into the role of astronomical
70 forcing in carbon-cycle perturbations.
71
72 **2. DEPOSITIONAL SETTING**
73 The Bohemian Cretaceous Basin formed as a continental through shallow-marine
74 siliciclastic system along reactivated, NW-trending faults of the Elbe fault zone
75 (Fig. 2; Uličný et al. 2009). The Cenomanian-Turonian interval is characterized
76 by a basinwide flooding and expansion of hemipelagic carbonates across the
77 basin. The overlying Turonian statigraphy consists predominantly of coarse-
78 grained progradational wedges of deltaic and nearshore siliciclastics (genetic
79 sequences TUR1-3; Uličný et al. 2009) that interfinger distally with offshore to
80 hemipelagic fines (Figs. S1-S6). Astronomical signals are best expressed in distal
81 parts of the siliciclastic depocenter where hemipelagic marlstones and
82 limestones (type A cycles; Figs. 3, S7 and S8) pass upward into offshore through
83 distal prodelta facies with cyclic variations in sand vs. mud contents (highlighted
84 by carbonate cementation; type B cycles; Figs. S7, S8).
85
86 **3. DATA AND METHODS**
87 **3.1. Data**

This study is based on subsurface data. An extensive borehole and well-log database provides a 3-dimensional stratigraphic framework (Uličný et al., 2009, 2014) and makes it possible to (i) trace changes in lithofacies and stratal geometries in the study area to determine the most suitable sites for time series analysis, and (ii) correlate biostratigraphic datums, carbon-isotope events and floating astrochronology across the basin (Figs. S1-S6).

All boreholes examined here exhibit long-term changes in sedimentation rate reflecting progradation of the marginal-marine siliciclastic system and shallowing of the coeval hemipelagic setting. Shorter-term fluctuations in sedimentation rates related to non-deposition and/or erosion across syndepositional faults are documented locally by angular relationships of well-log correlation markers (Figs. S1, S2). Boreholes suitable for time-series analysis and the construction of astronomical age model were selected from the prodeltaic zone based on two criteria: (i) The long-term change in sedimentation rate follows a simple pattern that can be modeled and removed numerically (e.g., linear change in sedimentation rate matched by a reciprocal function of signal wavelength in the depth-frequency plot; Fig. 4b). (ii) Short-term hiatuses and other fluctuations in sedimentation rates are absent or short relative to the tuning targets. The closest fit to these criteria is found in borehole J-719670 located ~5 km offshore from the progradational limit of sequence TUR2 (Fig. 2). Complementary analyses were executed on a series of other boreholes from the along-dip correlation profile. The list of key boreholes, their geographic coordinates and types of data are provided in Table S1.

Time-series analysis (section 3.4) was applied primarily to high-resolution resistivity logs that serve as a proxy for variations in sand/mud ratio

and carbonate cementation. The LL7 focused laterolog probe offers a favorable combination of sensitivity to dm- to meter-scale lithological variations in the mixed carbonate-siliciclastic strata, and noise attenuation (gamma-ray logs appear excessively noisy at the dm to meter scales as revealed by comparing closely spaced boreholes). The depth resolution of digitized resistivity logs is 10 cm, which in the reference borehole J-719670 corresponds to a minimum of 10 samples per the shortest (precessional) cycle discussed in this paper.

Isolated core samples from two boreholes (J-703684 and J-854604) and complete cores from boreholes 4523-A Sedlec and 4530-A Horní Beřkovice (Fig. 3) were available for a detailed examination of lithology and geochemistry. Greyscale-density profiles for the 4523-A Sedlec core were extracted from high-resolution (~10 pixels/mm) photographs using the image-processing software ImageJ (National Institutes of Health, Bethesda, MD).

3.2. Geochemistry

Samples from the 4523-A Sedlec and 4530-A Horní Beřkovice cores were analyzed for carbon-isotope composition of bulk organic carbon ($\delta^{13}C_{org}$). The measurements were performed in the Stable Isotope Laboratory of the Geological Survey, Prague (4523-A), and the Institute of Geochemistry, Mineralogy and Mineral Resources, Charles University, Prague (4530-A). Samples (10-15 g) were pulverized to an analytical-grade powder and decalcified using 10% HCl. Additional details are provided in Text S1. Data are reported relative to the Vienna Peedee Belemnite (VPDB) standard. Reproducibility of duplicate measurements was 0.12 ±0.08 (1σ) ‰ VPDB. The

temporal resolution of $\delta^{13}C_{org}$ data from the core 4523-A is 6.7 ±4.6 (1σ) kyr, according to the age model presented here.

Major and trace element concentrations were measured with an XRF spectrometer NITON XL3t GOLDD+; the XRF output was calibrated using 10 samples analyzed in an accredited laboratory of the Nanotechnology Centre, Technical University of Ostrava.

3.3. Chronostratigraphy, biostratigraphy

The Cenomanian/Turonian (C/T) boundary is constrained by a carbon-isotope correlation to the USGS #1 Portland core (Fig. S13) and well-log correlation of the base of ammonite Zone *Watinoceras devonense* from the Pecínov section, indicated there by the occurrence of inoceramid bivalve *Mytiloides puebloensis* (Fig. S4; cf. Košťák et al., 2018). The Lower Turonian ammonite Zone *Mammites nodosoides* is delineated by FO *M. nodosoides* at Pecínov (Košťák et al. 2018); a relatively large uncertainty in the correlation FO *M. nodosoides* and *W. devonense* to borehole 4523-A Sedlec (Fig. 3) is due to stratigraphic condensation at Pecínov (Figs. S4 and S13). The base of nannofossil Zone UC 7 which correlates above the base of the *M. nodosoides* Zone (Burnett 1998) is identified at approximately 178.75-181.75 m depth of the core 4523-A (Text S2). The first occurrence of the ammonite *Collignoniceras woollgari* (Mantell), which marks the Lower/Middle Turonian boundary (Ogg and Hinnov 2012), is correlated from borehole Nm-1 (Figs. S5, S6). The base of the Middle Turonian is further confirmed by the Lulworth carbon-isotope excursion (Jarvis et al. 2006; Fig. 1) identified in boreholes 4523-A and 4530-A (Fig. 3).

3.4. Time-series analysis and signal processing

Spectral estimates are calculated with the multitaper method (MTM; Thomson 1982) and evolutive harmonic analysis (EHA; Meyers et al. 2001). The statistical significance of the spectral results is quantified using the MTM harmonic F-test (Thomson 1982), and the assignment of spectral maxima to precessional, obliquity and eccentricity terms is verified with the Average Spectral Misfit (ASM; Meyers and Sageman 2007). Frequencies of orbital eccentricity for ASM analysis are estimated from the solutions La2010a through La2010d (Laskar et al. 2011a) following the approach of Malinverno et al. (2010) and Meyers et al. (2012b). Precessional and obliquity frequencies for ASM analysis are adopted from Waltham (2015). All ASM parameters are listed in Tables S2a and S2b. The TimeOpt method (Meyers 2015) is used to verify the correlation between the eccentricity signal and precessional envelope in selected intervals (Figs. S10, S11). All spectral estimates, ASM and TimeOpt calculations are conducted using the R package 'Astrochron', version 0.6 (Meyers, 2014; R Core Team, 2015). Signal filtering is performed with the Matlab script EPNOSE (Laurin et al. 2017) using a modification of the Taner filter (Taner 1992), which is symmetrical on a linear scale (Kodama and Hinnov 2014). Modulation envelopes were extracted with the Hilbert transform in the Matlab Signal Processing Toolbox; the algorithm is based on Marple (1999).

Data preparation included removal of a large-scale linear trend in sedimentation rate. This trend is manifested as a systematic drift in amplitude and F-test significance maxima approximating a reciprocal function of signal wavelength in the frequency domain (Figs. 4b and S9). To remove the linear trend, the depth scale of borehole J-719670 was modified by considering that the

mean spatial period of the precessional cycle evolved linearly from 1/1.05 m at the depth of 403 m to 1/0.32 m at the depth of 368 m (Fig. 4b), and setting this path to a constant value of 1/1.05 m (Fig. 4c). An analogous adjustment is applied to borehole J-650704, where a linear change from the period of 1/1.01 m at the depth of 428 m to the period of 1/0.35 m at the depth of 395 m is tuned to a constant period of 1/1.01 m. The resulting vertical scales are referred to as "detrended depth scales" in this paper (Figs. 4 and 5). Importantly, this type of linear pre-tuning is applied to an interval the time span of which greatly exceeds the period of short-eccentricity cycles (>300 kyr) and therefore should not distort the ~100-kyr modulation patterns examined in this study (section 4.2; cf. Zeeden et al. 2015). In order to reduce variance in the carbonate-rich interval of type A cyclicity, resistivity logs were converted to their common logarithm prior to time-series analysis. Additional details are provided in sections 4.1 through 4.4.

3.5 Astronomical solutions

Precessional and eccentricity signatures identified in this study are compared primarily with the astronomical solution La2010d (Laskar et al. 2011a), because this solution provides the most recent estimate for the precessional index (note that later solutions – Laskar et al. 2011b; Zeebe 2017; Zeebe and Lourens 2019 – are limited to eccentricity). The La2010d reconstructions of precessional index and obliquity have been obtained following the procedure described in Wu et al. (2013). We note, however, that all solutions available to date are unreliable in their prediction of Myr-scale eccentricity modulation beyond ~55 Myr ago (Laskar et al. 2011b; Zeebe 2017; Zeebe and Lourens 2019). No attempt is

212 therefore made in this study to pin the study interval to any particular segment
213 of the astronomical solution. The La2010d series is used primarily as a
214 constraint for the astronomical tuning target and its uncertainty. The solution
215 La2004 (Laskar et al. 2004) is shown for comparison, because, unlike La2010d, it
216 offers compatible eccentricity phases within the bounds of radioisotopic
217 uncertainty (±0.15 Myr, Meyers et al. 2012a) and provides the closes fit to Myr-
218 scale modulation in the Turonian interval (Ma et al. 2019).
219
220 **3.6 Age model**
221 Astrochronology is based on precessional and eccentricity signals identified in
222 the study interval. To estimate the uncertainty related to unstable astronomical
223 solutions, the interpreted precessional cycles are correlated to all segments of
224 the solution La2010d (Laskar et al., 2011a) between 89 and 99 Myr ago that are
225 compatible with eccentricity phasing in the study interval. Interpolation of the
226 age-depth relationships is based on the Bayesian approach and executed with
227 Bchron (Haslett and Parnell 2008). Further details are provided in section 4.4.
228
229 **3.7 Terminology**
230 The term "phasing" is used in this paper to refer to the timing of maxima and
231 minima of astronomical signals. An attempt is made to distinguish the phase of
232 the original astronomical forcing from the phase of filtered lithological or
233 geochemical proxies (through amplitude modulation and interference patterns
234 of precessional signals).
235 In a previous study, Laurin et al. (2016) use the term frequency
236 modulation (FM) to describe systematic changes in the frequency of

237 astronomical signals in depth-frequency plots (EHA). Although the EHA patterns
238 discussed here are analogous to Laurin et al.'s FM, a different term – interference
239 patterns (IP) - is used here to avoid confusion with FM examined by other
240 techniques (e.g., Liu et al. 1998; Hinnov 2000).
241
242 **4. RESULTS**
243 **4.1. Astronomical signatures**
244 Spectral estimates and interpretation of astronomical signatures focus on three
245 reference boreholes: J-719670, J-650704, and 4523-A (see Methods; Fig. 3).
246 Borehole J-719670 provides a well-preserved record for most of the Lower
247 Turonian, and is therefore considered the primary reference section. Results for
248 the lower and upper parts of the study interval are refined using data from
249 boreholes 4523-A and J-650704.
250
251 ***4.1.1. Borehole J-719670, resistivity***
252 Spectral estimates for a downhole resistivity log of this borehole show distinct
253 power-spectral and F-test significance maxima in the astronomical band (Fig. 4).
254 Power maxima exceeding the 90% significance level are labelled informally S_1
255 through S_4 and further discussed. A prominent cyclicity starts approximately 5 m
256 beneath the C/T boundary, with most variance located in the frequency band
257 ~0.25 cycle/m (~4 m period; S_2 in Fig. 4). Approximately 6 m above the C/T
258 boundary, the S_2 signal starts fading and the variance is transferred to higher
259 frequencies, namely S_4. This apparent increase in signal resolution follows
260 decreasing carbonate contents and the onset of siliciclastic-dominated (type B)
261 cyclicity that has a distinct response in the resistivity log. A refined, S_4-scale

262 resolution for the C/T boundary interval is obtained from greyscale data from
263 borehole 4523-A (section 4.1.3).
264 Further up-section, with an increase in siliciclastic contents related to
265 progradation of sequence TUR2, the S_4 trace in EHA plot drifts to lower
266 frequencies consistent with a linear increase in sedimentation rate (reciprocal
267 function of signal wavelength). Removal of the trend (explained in section 3.4
268 and Fig. 4b) makes it possible to examine the detailed structure of the S_4 band;
269 the signal is composed of two separate frequencies (labeled S_{4a} and S_{4b}) whose
270 interference is coherent with the S_2 cyclicity (Figs. 4, 5). ASM analysis (Fig. 4d)
271 suggests that the S_2 and S_4 signals correspond to cycles of orbital eccentricity
272 (97-127 kyr; related to g_4-g_5 and g_4-g_2) and climatic precession (~19–23 kyr),
273 respectively. The S_{4a} and S_{4b} components then correspond to the ~23-kyr (k+g_5
274 and k+g_2) and ~19-kyr (k+g_4 and k+g_3) terms of the precessional index,
275 respectively (where k refers to Earth's precession rate, and g_2 through g_5 are the
276 secular frequencies of planetary motion; Berger and Loutre 1990). A signature of
277 axial obliquity (S_3) is relatively weak and localized; where present, its variance
278 never exceeds variance of the precessional signal (variance ratio <0.7).
279 The EHA patterns (IP in Figs. 4 and 5) suggest well-preserved
280 precessional and eccentricity signals throughout most of the Lower Turonian.
281 Above the Lower/Middle Turonian boundary, however, the astronomical signals
282 become less distinct at the J-719670 site. In addition, the lowermost Turonian of
283 J-719670 exhibits minor condensation spanning marker bed 9 and
284 corresponding to one S_4 (precessional) cycle (Fig. S1). To confirm and refine the
285 estimate of astronomical cyclicity in these intervals, additional boreholes are
286 examined.

287

288 ***4.1.2. Borehole J-650704, resistivity***

289 This borehole is located approximately 4 km eastward of J-719670, closer to the
290 main siliciclastic depocenter of the Turonian depositional system (Fig. 2).
291 Proximity to the sediment source provides suitable conditions for the extension
292 of the S_4 signal into the Middle Turonian (Fig. 3). Spectral estimates for the
293 resistivity log reveal a pattern of S_2 and S_4 cyclicity, which is compatible with the
294 results for borehole J-719670 (Fig. 5).

295

296 ***4.1.3. Borehole 4523-A, greyscale***

297 Borehole 4523-A Sedlec is located down the depositional dip relative to
298 boreholes J-719670 and J-650704 (Fig. 2). Type B cyclicity, which consists
299 primarily of sand/mud alternations (Figs. S7, S8), is less well expressed in this
300 distal area due to reduced textural variability and local winnowing. However,
301 unlike resistivity logs of J-719670 and J-650704, the high-resolution greyscale
302 record of 4323-A makes it possible to resolve the S_4 signal in carbonate-rich
303 facies surrounding the C/T boundary (Fig. 6).

304

305 **4.2. Eccentricity phasing**

306 The initial information on the phasing of ~100-kyr and 405-kyr eccentricity
307 cycles is obtained from bandpassed resistivity logs following removal of a linear
308 trend in sedimentation rate (Fig. 5). The bandpassed signal, however, does not
309 reveal the phase relationship between the proxy and the eccentricity forcing. To
310 estimate the phase, we employ a suit of additional indices including (i) amplitude
311 modulation of bandpassed precessional signal (see section 4.2.1), and (ii)

preservation of interference patterns of the precessional signals in depth-frequency plots. Details on the interpretation are given below.

4.2.1. Short eccentricity (~100-kyr)

The inherent role of orbital eccentricity (e) in determining the impact of axial precession on insolation (quantified by the precessional index, e sinω, where ω is the longitude of the perihelion from the moving equinox) results in an eccentricity-paced modulation of the amplitude of precessional signals (e.g., Berger and Loutre 1991). This amplitude modulation has therefore been acknowledged as a tool to identify eccentricity maxima and minima (e.g., Herbert 1992; Grippo et al. 2004; Zeebe et al. 2017; Laurin et al. 2017). Any signals filtered from geological data are, however, prone to distortion due to sedimentation-rate instabilities and introduction of noise (both natural and analytical) into the filtered bandwidth. An accurate extraction of amplitude-modulated signals from stratigraphic data involves additional challenges such as frequency leakage out of the filtered bandwidth or introduction of harmonic tones into the filtered bandwidth due to short-term fluctuations in accumulation rates, diagenesis or differential compaction. The use of amplitude modulation therefore requires additional support. Here, the integrity of the precessional envelope is evaluated using interference patterns in EHA plot, analogous to the evaluation of 405-kyr phase in a previous study (Laurin et al. 2016).

The composition of fundamental frequencies of the main terms of short-eccentricity (g_4-g_2 and g_4-g_5) and precessional index ($k+g_5$, $k+g_2$, $k+g_4$ and $k+g_3$; Berger and Loutre 1990) links the interference of precessional terms to the eccentricity phase, i.e., $(k+g_4)-(k+g_2) = g_4-g_2$, and $(k+g_4)-(k+g_5) = g_4-g_5$. As

337 illustrated in Figure 5c, intervals of constructive interference of the ~19-kyr and
338 ~23-kyr terms mark short-eccentricity maxima, and intervals of destructive
339 interference are aligned with short-eccentricity minima. These patterns can be
340 examined in EHA plots that also make it possible to identify non-stationarities
341 and determine noise levels in the precessional band (see Laurin et al. 2016 for
342 illustration of possible modes of signal distortion and their EHA signatures).
343 In the resistivity log of J-719670, the interference patterns are well
344 preserved between correlation markers 10 and 37 (Fig. 4) suggesting that the
345 precessional signal and its amplitude modulation are not severely distorted in
346 this interval. The precessional envelope in J-719670 can also be extended some
347 distance beneath a minor hiatus near marker bed 9. The J-650704 record is
348 noisier, but exhibits interference patterns that are consistent with those in J-
349 719670 (Fig. 5). The amplitude envelope of S_4 signal in J-719670 is therefore
350 used in this study as the primary tool for the interpretation of short-eccentricity
351 maxima and minima. For intervals lacking a robust precessional modulation,
352 such as the Cenomanian/Turonian boundary interval, the short eccentricity
353 phases are estimated from a filtered S_2 signal, the polarity of which is confirmed
354 with the TimeOpt analysis (Figs. S10 and S11).
355 It should be noted that the above approach cannot resolve minor phase
356 differences and deformations that are to be expected in this depositional setting.
357 However, the method of astrochronological tuning applied here (section 4.4) is
358 not sensitive to minor lead/lag differences in the precessional and eccentricity
359 records; the phasing uncertainty is accommodated by the total uncertainty of the
360 age model.
361

362 ***4.2.2. Long eccentricity (405-kyr)***

363 The 405-kyr cycle, the rhythm of which is represented by signal S_1 (Fig. 4d), is
364 part of the same astronomical forcing as the ~100-kyr eccentricity term. The
365 preservation of its phase should therefore be analogous to the preservation of
366 short-eccentricity phase inferred in section 4.2.1. This means that maxima in the
367 filtered resistivity log should *approximate* the maxima in the original signal (as
368 noted above, minor phase uncertainties are accommodated by the tuning
369 approach). If so, then 405-kyr maxima should be located near marker beds 2a, 20
370 and 36 (Fig. 5). Support for this assumption can be sought in the modulation of
371 precessional and short-eccentricity signals.

372 As with the short-eccentricity phasing, the phase of 405-kyr eccentricity
373 (g_2-g_5) is involved in the interference of precessional terms. In this case, however,
374 the interpretation in real stratigraphic data would require an exceptionally clear
375 signal permitting separation of the 23.05-kyr (k+g_5) and ~21.81-kyr (k+g_2)
376 precessional terms (Tab. S2a). In spite of an excellent signal preservation, these
377 components cannot be resolved in the study interval. Other indices are therefore
378 required.

379 Pronounced amplitude modulation and well-developed interference
380 patterns in the precessional band can be expected to form preferably during
381 405-kyr maxima, as in the theoretical solutions. The nodes in 405-kyr
382 eccentricity, in contrast, should exhibit relatively weak precessional signals and
383 indistinct interference patterns in time-frequency plots (Fig. 5c). Following these
384 assumptions, 405-kyr maxima should be centered between marker beds 17 – 21
385 and near markers 36 – 37, in agreement with the S_1 bandpass (Fig. 5a,b). This
386 interpretation is further supported by a transient record of eccentricity in the

Lower/Middle Turonian boundary interval in borehole Bch-1 (central part of the basin; Figs. 7a and S12).

Modulation of the short-eccentricity signal (S_2) is of limited use due to an upward decline in its power. Gradual facies change above marker bed 2b (Fig. S7) and local winnowing of marker bed 9 (Fig. 5) also corrupt the S_1 bandpass in the lower part of the study interval. To preserve a realistic, ~1:4 bundling of short-eccentricity vs. long-eccentricity cycles, the lowermost maximum of the 405-kyr eccentricity should be located some distance above the lowermost maximum of the S_1 bandpass, between markers 2b and 3 (between short-eccentricity maxima ecc2 and ecc3; Figs. 5 and 7).

The final support for the interpretation of 405-kyr phase comes from bundling ratios of short-eccentricity vs. precessional cycles that are controlled chiefly by changes in the instantaneous period of short-eccentricity cycles. The 405-kyr minima are typically associated with low instantaneous periods (as low as 77 kyr; Hinnov 2000) and low bundling ratios (as low as 1:3 during ~2.4-Myr nodes). In the study interval, the bundling ratios range from 3.5 to 5.7 with minima near marker beds 7 and 31, coincident with 405-kyr minima predicted by the S_1 bandpass and precessional interference patterns (Fig. 7).

4.3. Myr-scale eccentricity

The ~2.4-Myr modulation of orbital eccentricity related to the precession of perihelia of Earth and Mars ($g_4 - g_3$; Laskar et al. 2004) cannot be interpreted directly due to uncertainties in astronomical solutions and a relatively short time span of the study interval (~1 Myr). However, since long-term eccentricity minima exhibit suppressed ~100-kyr modulations (Fig. 5c; cf. Hinnov 2000), the

412 exquisite preservation of ~100-kyr interference patterns in the middle part of
413 the Lower Turonian and lower part of the Middle Turonian makes it possible to
414 infer a broadly defined ~2.4-Myr maximum in this interval. Such a phasing
415 implies a ~2.4-Myr node overlapping with OAE II, in agreement with the results
416 of previous studies (Batenburg et al. 2016; Laurin et al. 2016; Ma et al. 2019).
417
418 **4.4 Age model**
419 The study interval spans twelve short-eccentricity cycles labelled ecc1 through
420 ecc11 (a minor cycle at 405-kyr minimum is labelled ecc3b; Fig. 7). These cycles,
421 combined with the precessional cyclicity, provide the basis for the construction
422 of floating age model. The key issue affecting accuracy of the age estimate is the
423 selection of tuning targets for the eccentricity and precessional signals. A
424 constant tuning target, e.g., 95 kyr for short eccentricity, can be considered
425 inaccurate, because the instantaneous period of this cycle varies significantly in
426 the course of 405-kyr and Myr-scale modulations (e.g., Hinnov 2000). Tuning to a
427 particular segment of an astronomical solution would settle this issue, but all
428 astronomical solutions available to date are unreliable in their prediction of Myr-
429 scale eccentricity modulation beyond ~55 Myr ago (Laskar et al. 2011a,b; Zeebe
430 2017; Zeebe and Lourens 2019). To estimate the uncertainty associated with
431 Myr-scale modulation, we select a 10-Myr interval of the solution La2010d
432 centered at 94 Myr ago (~C/T boundary) and tune the observed signals to every
433 compatible segment of the theoretical solution in this interval.
434 The tuning is performed by linking individual S_4 cycles with precessional
435 cycles of the La2010d solution (Laskar et al. 2011a) within the framework of
436 ~100-kyr (S_2) and 405-kyr (S_1) maxima and minima interpreted in section 4.2. In

437 this concept, the precessional cycles provide the temporal resolution and
438 eccentricity cycles provide stability (by, for example, identifying missing
439 precessional beats at eccentricity minima). Each tuning assigns floating ages to
440 correlation markers 1 through 43, which are manifestations of the precessional
441 (S_4) cyclicity (Figs. S14 and S15). The mean and standard deviation of the
442 floating ages, calculated from the total number of tuned segments (n=21),
443 constitute the nominal age model and uncertainty of the tuning target (Tab. S3).
444 An interpolation of the nominal age model to chronostratigraphic
445 boundaries using the Bayesian approach (Haslett and Parnell 2008; Text S3)
446 suggests an 885 kyr duration for the Early Turonian. The uncertainty of this time
447 span is estimated as ±41 kyr (95% confidence interval) by combining the
448 uncertainty of the location of chronostratigraphic boundaries (Fig. 3) and the
449 uncertainty of the La2010d tuning target (Tab. 2). The age model also quantifies
450 the timing of eccentricity maxima and minima (Fig. 8): the
451 Cenomanian/Turonian boundary predates the first Turonian 405-kyr maximum
452 by 82 ±70 (2σ) kyr, and the Early/Middle Turonian boundary coincides with the
453 third Turonian 405-kyr maximum within the uncertainty (2σ = 70 kyr).
454
455 **4.5 Age-calibrated $\delta^{13}C$**
456 The Bayesian interpolation is further applied to estimate floating ages of carbon-
457 isotope samples in borehole 4523-A (Fig. 8). This age calibration suggests that
458 the negative shift in $\delta^{13}C$ following OAE II is superimposed upon increasing 405-
459 kyr eccentricity. The temporal distribution of small-scale anomalies
460 approximates a ~110-kyr pacing in the lowermost Turonian, but passes to a
461 longer, ~170-kyr pattern towards the Middle Turonian (Fig. 8d).

462

463 **5. DISCUSSION**

464 **5.1 Chronology of the Early Turonian**

465 The floating-age estimate presented here falls within the range presented in
466 previous studies (Tab. 1). It is most closely compatible with astrochronology of
467 the Wunstorf core (Voigt et al. 2008), with which it shares the precession-scale
468 resolution. The minor difference in the duration of Early Turonian between these
469 models (<50 kyr) might be related to the selection of monochromatic
470 precessional tuning target (21 kyr) and the loss of precessional signal in the
471 uppermost part of the Lower Turonian at Wunstorf. Another robust estimate, the
472 Portland time scale of Meyers et al. (2001, 2012a) and Sageman et al. (2006),
473 appears ~100 kyr short compared to the Bohemian model. The difference is
474 again possibly related to the use of a monochromatic tuning target, in this case
475 the 95 kyr for short eccentricity in Portland (note that the use of mean short-
476 eccentricity period of 110 kyr would increase the duration estimate by 16%,
477 matching the Bohemian estimate within its uncertainty). Other published
478 astrochronologies are difficult to assess due uncertainties in the definition of
479 chronostratigraphic boundaries in the Bottaccione (Sprovieri et al. 2013),
480 Contessa (Batenburg et al. 2016) and Iona (Eldrett et al. 2015) records.

481 When anchored to the C/T boundary age of 93.9 ±0.15 Myr ago (Meyers
482 et al. 2012a), the above model gives the age of the Early/Middle Turonian
483 boundary as 93.02 ±0.16 (2σ) Myr ago. Alternatively, the age of 93.07 ±0.06 (2σ)
484 Myr ago is obtained by anchoring to 93.95 ±0.05 Myr ago (Jones et al. 2020).

485

486 **5.2 Eccentricity phasing in the Cenomanian–Turonian interval**

The inferred ~2.4-Myr node in eccentricity modulation during OAE II and a long-term increase in the eccentricity amplitudes towards the Middle Turonian are in agreement with previous results supporting the role of increasing seasonality in the recovery from OAE II (Batenburg et al. 2016; Laurin et al. 2016). The 405-kyr phasing, in contrast, cannot be compared directly with previous studies due to uncertainties in stratigraphic correlation to published sections (Figs. 1 and S17) and a lack of direct phase constraints across OAE II. Well-preserved astronomical signals allowing a robust interpretation of the 405-kyr phases have been described from the pre-OAE II interval at Furlo (Batenburg et al. 2016; Laurin et al. 2016). When extrapolating eccentricity cycles of the Bohemian record to the base of OAE II using published astrochronologies (Sageman et al. 2006; Ma et al. 2014; Fig. S13), the 405-kyr maxima appear over 90 kyr (>80°) out-of-phase relative to the Furlo record (Fig. 8c). Considering that both the Early Turonian and pre-OAE II eccentricity records are robust, the most likely source of error is in the extrapolation across OAE II. Possible explanations include (i) non-deposition or condensation near the base of Livello Bonarelli at Furlo, (ii) a minor underestimation of the eccentricity target period in the OAE II chronology (see section 5.1), or (iii) potential diachroneity of biostratigraphic markers between the C/T boundary stratotype and Europe (Boulila et al. 2020).

Another apparent mismatch is found in the Early Turonian, when comparing the Bohemian 405-kyr record with eccentricity maxima inferred for the Contessa section (Batenburg et al. 2016; Figs. 1f and S17). The two records can, however, be aligned with each other when considering a ±150 kyr uncertainty for the Contessa section (Batenburg et al. 2016) and delineating the Cenomanian/Turonian boundary as in Wendler (2013) (Fig. S17).

512 Using a cosine approximation of the g_2-g_5 metronome (as recommended
513 by Laskar 2020; equation 4.10 in GTS 2020), the earliest Turonian maximum of
514 405-kyr eccentricity corresponds to the cycle no. 232. The results presented here
515 provide a feedback to astronomical solutions by constraining the age of this 405-
516 kyr maximum to 93.87 ±0.09 (2σ) Myr ago, when anchored to the refined C/T
517 boundary age of 93.95 ±0.05 Myr ago (Jones et al. 2020). The eccentricity
518 maximum no. 230, which coincides with the Early/Middle Turonian boundary, is
519 then dated as 93.06 ±0.09 (2σ) Myr ago.
520
521 **5.3 Short-term $\delta^{13}C$ anomalies: interbasinal correlation**
522 Comparison with the age-calibrated record of Wunstorf (Voigt et al. 2008)
523 suggests that the most likely candidate for the Holywell CIE is the excursion "se-
524 6" or "se-10". The timing of the Holywell anomaly in the reference section of
525 English Chalk (Jarvis et al. 2006) appears younger even with the updated age of
526 the Early/Middle Turonian boundary (Fig. 8e). Since biostratigraphic arguments
527 for the correlation of Holywell CIE to Münsterland and Lower Saxony have been
528 presented by Voigt et al. (2007, 2008), the mismatch is most likely attributed to
529 the scarcity of age-control points in the English Chalk record and uncertain
530 dating of FO *M. nodosoides* (Fig. 8e).
531 In general, a correlation of small-scale CIEs that lack a distinct structure
532 or magnitude will remain ambiguous without biostratigraphic constraints or
533 detailed age calibration of both the reference section and the correlated section.
534 The original depth-domain profiles and time-domain profiles interpolated across
535 large intervals can provide misleading information about the relative spacing of

536 CIEs due to unrecognized changes in sedimentation rates and distorted age-
537 depth relationships.
538
539 **5.4 Short-term $\delta^{13}C$ anomalies: timing and origin**
540 The ~100-kyr recurrence interval of short-term $\delta^{13}C$ anomalies in the earliest
541 Turonian (Fig. 8) points to the possible influence of eccentricity-modulated
542 seasonal insolation intensities on the carbon-cycle budget (cf. Berger et al. 1993).
543 The $\delta^{13}C$ signature is, however, not strictly coherent with inferred short-
544 eccentricity cycles (Fig. 6) suggesting a causal mechanism different from that
545 proposed for other greenhouse intervals, e.g., Paleocene-Eocene (Cramer et al.
546 2003; Zeebe et al. 2017). The observed incoherency may point to the
547 heterogeneous composition of carbon sources and sinks, involving sensitivity to
548 different aspects of the insolation control (e.g., seasonal intensity vs. integrated
549 seasonal insolation) and geographic locations. The possible role of high- or mid-
550 latitude carbon reservoirs responding to meridional insolation gradients (cf.
551 Raymo and Nisancioglu 2003) or integrated summer insolation (cf. Huybers
552 2006) is apparent in the transition towards ~170-kyr pacing of $\delta^{13}C$ anomalies in
553 the mid Early Turonian (Fig. 8d). The ~170-kyr term occurs in amplitude
554 modulation of axial obliquity (Hinnov 2000; Fig. S16) and its record in the
555 isotopic balance of the carbon cycle can be amplified by the ~100-kyr residence
556 time of carbon (Kump and Arthur 1999), analogous to the amplification of
557 eccentricity terms from precessional modulation (e.g., Short et al. 1991; Herbert
558 1997).
559 Notably, the transition from short-eccentricity pacing to ~170-kyr pacing
560 is superimposed upon the rising phase of long-term eccentricity modulation

(Figs. 5 and 8b). The loss of eccentricity pacing of $\delta^{13}C$ excursions can therefore not be attributed to the inherent change in eccentricity amplitudes. To produce the observed pattern, the carbon-cycle perturbations must have decoupled from low-latitude seasonal insolation involving carbon storage in the monsoonal belt (cf. Rossignol-Stricks 1983). The main control on carbon-isotope mass balance was transferred to mid- to high-latitudes during this interval, paralleling a Myr-scale, obliquity-paced carbon exchange inferred in previous studies (Wendler et al. 2014; Laurin et al. 2015) and the onset of long-term cooling of surface temperatures (cf. Pucéat et al. 2003; Friedrich et al. 2012).

SUMMARY

1. The record of precessional and eccentricity cycles in the Bohemian Cretaceous Basin constrains the duration of Early Turonian to 885 ±41 (2σ) kyr. Numerical age of the Early/Middle Turonian boundary is 93.07 ±0.06 (2σ) Myr ago (when anchored to C/T boundary age of 93.95 ±0.05 Myr ago; Jones et al. 2020).
2. The Cenomanian/Turonian boundary precedes the first Turonian 405-kyr maximum by 82 ±70 (2σ) kyr. The age of this eccentricity maximum, no. 232 in the metronomic sequence (Laskar 2020), is estimated as 93.87 ±0.09 (2σ) Myr ago (anchored to C/T boundary age of 93.95 ±0.05 Myr ago; Jones et al. 2020).
3. The recovery from OAE II is superimposed upon rising phases of 405-kyr and ~2.4-Myr eccentricity. The ~2.4-Myr cycle peaks between late Early Turonian and early Middle Turonian.

4. Astronomical control on the post-OAE II carbon cycle is documented by ~110-kyr pacing of $\delta^{13}C$ anomalies, which gives way to ~170-kyr obliquity pattern during the mid Early Turonian. The transition suggests decoupling of the carbon-cycle mass balance from low-latitude seasonal insolation and increasing role of high latitude carbon reservoirs.

ACKNOWLEDGMENTS

This research was supported by the Czech Science Foundation (GAČR) project No. 17-10982S, research program RVO 67985530 of the Czech Academy of Sciences of the Czech Republic, and research program RVO 67985831 of the Czech Geological Survey. Acquisition of digital well-log data and core samples was made possible through cooperation with DIAMO, s.p. and the Czech Geological Survey. We are particularly grateful for help with data acquisition to Roland Nádaskay, Jaroslav Valečka, Pavel Veselý, and Dana Čápová. Lukáš Hronec assisted with core preparation and sampling. Comments by Silke Voigt, David De Vleeschouwer, and an anonymous reviewer helped considerably to improve the first version of this paper.

DATA AVAILABILITY

Data discussed in this paper are provided in the Supplementary Information, Datasets S1 through S5. By the time this article is accepted for publication, all data will be deposited in the Pangaea Data Publisher.

607 **REFERENCES**

608 Batenburg, S. J., D. De Vleeschouwer, M. Sprovieri, F. J. Hilgen, A. S. Gale, B. S.
609 Singer, C. Koeberl, R. Coccioni, P. Claeys, and A. Montanari (2016), Orbital
610 control on the timing of oceanic anoxia in the Late Cretaceous. Clim. Past,
611 12, 1995-2009, doi:10.5194/cp-12-1995-2016.

612 Berger, A.., and M. F. Loutre (1990), Origine des fréquences des éléments
613 astronomiques intervenant dans le calcul de l'insolation. Bulletin de la
614 Classe des sciences, tome 1. pp. 45-106, doi:10.3406/barb.1990.38523

615 Berger, A., and M. F. Loutre (1991), Insolation values for the climate of the last 10
616 million years, Quat. Sci. Rev. 10, 297–317.

617 Berger, A., M. F. Loutre, and C. Tricot (1993), Insolation and Earth's orbital
618 periods. Journal of Geophysical Research, 98 (D6), 10,341–10,362,
619 doi:10.1029/93JD00222.

620 Boulila, S., Charbonnier, G., Spangenberg, J. E., Gardin, S., Galbrun, B., Briard, J., Le
621 Callonnec, L. (2020), Unraveling short- and long-term carbon cycle
622 variations during the Oceanic Anoxic Event 2 from the Paris Basin Chalk.
623 Global and Planetary Change, 186, 103126, doi:
624 10.1016/j.gloplacha.2020.103126

625 Burnett, J.A. (1998), Upper Cretaceous. In: Calcareous Nannofossil
626 Biostratigraphy (P.R. Bown), 132–199. British Micropalaeontological
627 Society, London.

628 Čech, S., V. Klein, J. Kříž, and J. Valečka (1980), Revision of the Upper Cretaceous
629 stratigraphy of the Bohemian Cretaceous Basin, Věst. Ústřed. Úst. Geol.
630 (Bull. Geol. Surv. Prague), 55, 277–296.

631 Clarke, L. J., and H. C. Jenkyns (1999), New oxygen isotope evidence for long-term
632 Cretaceous climatic change in the Southern Hemisphere, Geology, 27,
633 699–702, doi:10.1130/0091-7613(1999)027<0699:NOIEFL>2.3.CO;2.
634 Cramer, B. S., J. D. Wright, D. V. Kent, and M. P. Aubry (2003), Orbital climate
635 forcing of $\delta^{13}C$ excursions in the late Paleocene–early Eocene (chrons
636 C24n–C25n), Paleoceanography, 18, 1097, doi:10.1029/2003PA000909.
637 Du Vivier, A. D. C., D. Selby, B. B. Sageman, I. Jarvis, D. R. Gröcke, and S. Voigt, S.
638 (2014), Marine $^{187}Os/^{188}Os$ isotope stratigraphy reveals the interaction of
639 volcanism and ocean circulation during Oceanic Anoxic Event 2, Earth
640 Planet. Sc. Lett., 389, 23-33, doi:10.1016/j.epsl.2013.12.024.
641 Eldrett, J.S., Ma, C., Bergman, S.C., Lutz, B., Gregory, F.J., Dodsworth, P., Phipps, M.,
642 Hardas, P., Minisini, D., Ozkan, A., Ramezani, J., Bowring, S.A., Kamo, S.L.,
643 Ferguson, K., Macaulay, C., and Kelly, A.E. (2015), An astronomically
644 calibrated stratigraphy of the Cenomanian, Turonian and earliest
645 Coniacian from the Cretaceous Western Interior Seaway, USA: Im-
646 plications for global chronostratigraphy. Cretaceous Research, v. 56, p.
647 316–344, https://doi.org/10.1016/j.cretres.2015.04.010.
648 Friedrich, O., Norris, R.D., and Erbacher, J. (2012), Evolution of middle to Late
649 Cretaceous oceans—A 55 m.y. record of Earth's temperature and carbon
650 cycle, Geology, 40, 107–110, doi:10.1130/G32701.1.
651 Gale, A.S, Mutterlose, J., Batenburg, S., Gradstein, F.M., Agterberg, F.P., Ogg, J.G.,
652 and Petrizzo, M.R. (2020), The Cretaceous Period, *in* Gradstein, F.M., Ogg,
653 J.G., Schmitz, M.D., Ogg, G.M., eds., The Geologic Time Scale 2020, Boston,
654 Massachusetts, Elsevier, p. 1023-1086, doi:10.1016/B978-0-12-824360-
655 2.00027-9.

656 Grippo, A., Fischer, A.G., Hinnov, L.A., Herbert, T.D., Premoli Silva, I. (2004),
657 Cyclostratigraphy and chronolo- gy of the Albian stage (Piobbico Italy). In:
658 D'Argenio, B. et al. (Eds.), Cyclostratigraphy: Approaches and Case
659 Histories. Special Publication SEPM (Society for Sedi- mentary Geology)
660 81, 57–81.
661 Hinnov, L.A. (2000), New perspectives on orbitally forced stratigraphy: Annual
662 Review of Earth and Planetary Sciences, 28, 419–475.
663 Haslett, J., & Parnell, A. (2008), A simple monotone process with application to
664 radiocarbon-dated depth chronologies. Journal of the Royal Statistical
665 Society: Series C (Applied Statistics), 57(4), 399–418.
666 Hay, W. W., R. M. DeConto, C. N. Wold, K. M. Wilson, S. Voigt, M. Schulz, A. Wold-
667 Rossby, W.-C. Dullo, A. B. Ronov, A. N. Balukhovsky, and E. Söding (1999),
668 Alternative global Cretaceous paleogeography, in Evolution of the
669 Cretaceous Ocean-Climate System, Geol. Soc. Am. Special Paper 332,
670 edited by E. Barrera and C. C. Johnson, 1-47, Boulder, Colorado.
671 Herbert, T.D. (1992), Paleomagnetic calibration of Milankovitch cyclicity in
672 Lower Cretaceous sediments. Earth. Planet. Sci. Lett,. 112, 15–28.
673 Herbert, T. D. (1997), A long marine history of carbon cycle modulation by
674 orbital-climatic changes. Proceedings of the National Academy of Sciences
675 of the United States of America, 94(16), 8362–8369. doi:
676 10.1073/pnas.94.16.8362
677 Huybers, P. J. (2006), Early Pleistocene glacial cycles and the integrated summer
678 insolation forcing, Science, 313, 508–511, doi:10.1126/ science.1125249.

679 Jones, C.E., and Jenkyns, H.C. (2001), Seawater strontium isotopes, Oceanic
680 Anoxic Events, and seafloor hydrothermal activity in the Jurassic and
681 Cretaceous. American Journal of Science, 301, 112–149.
682 Jones, M.M., Sageman, B.B., Selby, D., Jicha, B.R., Singer, B.S., and Titus, A.L. (2020),
683 Regional chronostratigraphic synthesis of the Cenomanian-Turonian
684 Oceanic Anoxic Event 2 (OAE2) interval, Western Interior Basin (USA):
685 New Re-Os chemostratigraphy and $^{40}Ar/^{39}Ar$ geochronology. GSA Bulletin
686 2020; doi: 10.1130/B35594.1
687 Joo, Y. J., and B. B. Sageman (2014), Cenomanian to Campanian carbon isotope
688 chemostratigraphy from the Western Interior Basin, U.S.A., J. Sediment.
689 Res., 84, 529-542, doi:10.2110/jsr.2014.38.
690 Jarvis, I., A. S. Gale, H. C. Jenkyns, and M. A. Pearce (2006), Secular variation in
691 Late Cretaceous carbon isotopes and sea-level change: evidence from a
692 new d13C carbonate reference curve for the Cenomanian – Campanian
693 (99.6 – 70.6 Ma), Geol. Mag., 143, 561–608.
694 Jarvis, I., J. Trabucho-Alexandre, D. R. Gröcke, D. Uličný, and J. Laurin (2015),
695 Intercontinental correlation of organic carbon and carbonate stable
696 isotope records: evidence of climate and sea-level change during the
697 Turonian (Cretaceous), The Depositional Record, 1, 53-90,
698 doi:10.1002/dep2.6.
699 Kodama, K. P., and Hinnov, L. A. (2014), Rock magnetic cyclostratigraphy. Oxford,
700 UK: Wiley-Blackwell. https://doi.org/10.1002/9781118561294
701 Košťák, M., Čech, S., Uličný, D., Sklenář, J., Ekrt, B., and Mazuch, M. (2018),
702 Ammonites, inoceramids and stable carbon isotopes of the
703 CenomanianeTuronian OAE2 interval in central Europe: Pecínov quarry,

704 Bohemian Cretaceous Basin (Czech Republic). Cretaceous Research, 87,
705 150-173.
706 Kump, L. R., and M. A. Arthur (1999), Interpreting carbon–isotope excursions:
707 Carbonate and organic matter, Chem. Geol., 161, 181–198,
708 doi:10.1016/S0009-2541(99)00086-8.
709 Laskar, J. (2020), Astrochronology, *in* Gradstein, F.M., Ogg, J.G., Schmitz, M.D., Ogg,
710 G.M., eds., The Geologic Time Scale 2020, Boston, Massachusetts, Elsevier,
711 p. 139-158, doi:10.1016/B978-0-12-824360-2.00004-8.
712 Laskar, J., P. Robutel, F. Joutel, M. Gastineau, A.C.M. Correia, and B. Levrard
713 (2004), A long-term numerical solution for the insolation quantities of the
714 Earth, Astron. Astrophys., 428, 261–285, doi:10.1051/0004-
715 6361:20041335.
716 Laskar, J., Fienga, A., Gastineau, M., and Manche, H. (2011a), La2010: A new
717 orbital solution for the long term motion of the Earth: Astronomy and
718 Astrophysics, 532, A89, doi:10.1051/0004-6361/201116836.
719 Laskar, J., Gastineau, M., Delisle, J-B., Farrés, A., and Fienga, A. (2011b), Strong
720 chaos induced by close encounters with Ceres and Vesta: Astronomy and
721 Astrophysics, 532, L4, doi: 10.1051/0004-6361/201117504.
722 Laurin, J., Meyers, S.R., Galeotti, S., and Lanci, L. (2016), Frequency modulation
723 reveals the phasing of orbital eccentricity during Cretaceous Oceanic
724 Anoxic Event II and the Eocene hyperthermals. Earth and Planetary
725 Science Letters, 442, 143-156, doi:10.1016/j.epsl.2016.02.047.
726 Laurin, J., S. R. Meyers, D. Uličný, I. Jarvis, and B. B. Sageman (2015), Axial
727 obliquity control on the greenhouse carbon budget through middle- to

728 high-latitude reservoirs, Paleoceanography, 30, 133-149,
729 doi:10.1002/2014PA002736
730 Laurin, J., Růžek, B., and Giorgioni, M. (2017), Orbital signals in carbon isotopes:
731 phase distortion as a signature of the carbon cycle. Paleoceanography, 32,
732 1236–1255. doi: 10.1002/2017PA003143
733 Liu, H.S. (1998), Glacial-interglacial changes induced by pulse modulation of the
734 incoming solar radiation. J. Geophys. Res. 103(D20), 26147–26164.
735 Ma, C., S. R. Meyers, B. B. Sageman, B. S. Singer, and B. R. Jicha (2014), Testing the
736 astronomical time scale for oceanic anoxic event 2, and its extension into
737 Cenomanian strata of the Western Interior Basin (USA), Geol. Soc. Am.
738 Bul., 126, 974-989.
739 Ma, C., Meyers, S.R., and Sageman, B.B. (2019), Testing Late Cretaceous
740 astronomical solutions in a 15 million year astrochronologic record from
741 North America. Earth and Planetary Science Letters, 513, 1-11.
742 Malinverno, A., E. Erba, and T. Herbert (2010), Orbital tuning as an inverse
743 problem: Chronology of the early Aptian oceanic anoxic event 1a (Selli
744 Level) in the Cismon APTICORE, Paleoceanography, 25, PA2203,
745 doi:10.1029/2009PA001769.
746 Marple, S. L. (1999), Computing the discrete-time analytic signal via FFT. IEEE
747 Transactions on Signal Processing, 47(9), 2600–2603,
748 doi:10.1109/78.782222.
749 Meyers, S. R. (2014), astrochron: An R Package for Astrochronology (Version
750 0.3.1). http://www.geology.wisc.edu/~smeyers.
751 Meyers, S.R. (2015), The evaluation of eccentricity-related amplitude modulation
752 and bundling in paleoclimate data: An inverse approach for

753 astrochronologic testing and time scale optimization: Paleoceanography,
754 30, doi:10.1002/2015PA002850.
755 Meyers, S. R., S. E. Siewert, B. S. Singer, B. B. Sageman, D. J. Condon, J. D.
756 Obradovich, B. R. Jicha, and D. A. Sawyer (2012a), Intercalibration of
757 radioisotopic and astrochronologic time scales for the Cenomanian-
758 Turonian boundary interval, Western Interior Basin, USA, Geology, 40, 7-
759 10, doi:10.1130/G32261.1.
760 Meyers, S. R., B. B. Sageman, and M. A. Arthur (2012b), Obliquity forcing of
761 organic matter accumulation during Oceanic Anoxic Event 2,
762 Paleoceanography, 27, PA3212, doi:10.1029/2012PA002286.
763 Meyers, S.R., Sageman, B.B., and Hinnov, L.A. (2001), Integrated quantitative
764 stratigraphy of the Cenomanian-Turonian Bridge Creek Limestone
765 Member using evolutive harmonic analysis and stratigraphic modeling:
766 Journal of Sedimentary Research, 71, 628-644.
767 Meyers, S.R., and Sageman, B.B. (2007), Quantification of deep-time orbital
768 forcing by average spectral misfit: American Journal of Science, 307, 773–
769 792, doi:10.2475/05.2007.01.
770 Ogg, J.G., and Hinnov, L.A. (2012), Cretaceous, *in* Gradstein, F.M., Ogg, J.G., Schmitz,
771 M.D., and Ogg, G.M., eds., The Geologic Time Scale 2012: Boston,
772 Massachusetts, Elsevier, p. 793–853, doi:10.1016/B978-0-444-59425-
773 9.00027-5.
774 Pearce, M.A., Jarvis, I., Ball, P.J., and Laurin, J. (2020), Palynology of the
775 Cenomanian to lowermost Campanian (Upper Cretaceous) Chalk of the
776 Trunch Borehole (Norfolk, UK) and a new dinoflagellate cyst bioevent

777 stratigraphy for NW Europe. Review of Palaeobotany and Palynology, 278,
778 104188, doi:10.1016/j.revpalbo.2020.104188.
779 Pucéat, E., C. Lecuyer, S. M. F. Sheppard, G. Dromart, S. Reboulet, and P. Grandjean
780 (2003), Thermal evolution of Cretaceous Tethyan marine waters inferred
781 from oxygen isotope composition of fish tooth enamels,
782 Paleoceanography, 18 (2), 1029, doi:10.1029/2002PA000823.
783 Raymo, M. E., and K. Nisancioglu (2003), The 41 kyr world: Milankovitch's other
784 unsolved mystery, Paleoceanography, 18(1), 1011,
785 doi:10.1029/2002PA000791.
786 R Core Team (2015), R: A language and environment for statistical computing. R
787 Foundation for Statistical Computing, Vienna, Austria. http://www.R-
788 project.org/.
789 Rossignol-Strick, M. (1983), African monsoons, an immediate climate response
790 to orbital insolation. Nature 304, 46–49.
791 Sageman, B. B., S. R. Meyers, and M. A. Arthur (2006), Orbital time scale and new
792 C-isotope record for Cenomanian-Turonian boundary stratotype, Geology,
793 34, 125-125.
794 Schlanger, S., Jenkyns, H. (1976). Cretaceous oceanic anoxic events: causes and
795 consequences. Geol. Mijnb. 55, 179–184.
796 Short, D. A., J. G. Mengel, T. J. Crowley, W. T. Hyde, and G. R. North (1991),
797 Filtering of Milankovitch cycles by Earth's geography, Quat. Res., 35, 157–
798 173, doi:10.1016/0033-5894(91)90064-C.
799 Sprovieri, M., N. Sabatino, N. Pelosi, S. J. Batenburg, R. Coccioni, M. Iavarone, and
800 S. Mazzola (2013), Late Cretaceous orbitally-paced carbon isotope
801 stratigraphy from the Bottaccione Gorge (Italy), Palaeogeogr.,

802 Palaeoclimatol. Palaeoecol., 379–380, 1–94,
803 doi:10.1016/j.palaeo.2013.04.006.
804 Stoll, H. and Schrag, D. (2000), High-resolution stable isotope records from the
805 Upper Cretaceous rocks of Italy and Spain: Glacial episodes in a
806 greenhouse planet? Geol. Soc. Am. Bull., 112, 308–319.
807 Taner, M. T. (1992), Attributes revisited, technical publication. Rock solid images,
808 Inc., Houston, TX. Retrieved from http://rocksolidimages.
809 com/pdf/attrib_revisited.htm (updated 2003).
810 Thomson, D.J. (1982), Spectrum estimation and harmonic analysis: Proc. IEEE, v.
811 70, p. 1055–1096.
812 Uličný, D., Laurin, J., and Čech, S. (2009), Controls on clastic sequence geometries
813 in a shallow- marine, transtensional basin: the Bohemian Cretaceous
814 Basin, Czech Republic: Sedimentology, 56, 1077–1114.
815 Uličný, D., Jarvis, I., Gröcke, D.R., Čech, S., Laurin, J., Olde, K., Trabucho-Alexandre,
816 J., Švábenická, L. and Pedenychouk, N. (2014), A high-resolution carbon-
817 isotope record of the Turonian stage correlated to a siliciclastic basin fill:
818 Implications for mid-Cretaceous sea-level change: Palaeogeography
819 Palaeoclimatology Palaeoecology, 405, 42–58.
820 Voigt, S., J. Erbacher, J. Mutterlose, W. Weiss, T. Westerhold, F. Wiese, M. Wilmsen,
821 T. Wonik (2008), The Cenomanian–Turonian of the Wunstorf section
822 (North Germany): global stratigraphic reference section and new orbital
823 time scale for Oceanic Anoxic Event 2, Newslett. Stratigr., 43, 65–89.
824 Voigt, S., Aurag, A., Leis, F. and Kaplan, U. (2007), Late Cenomanian to Middle
825 Turonian high-resolution carbon isotope stratigraphy: new data from the
826 Münsterland Cretaceous Basin, Germany. Earth Planet. Sci. Lett., 253, 196.

827 Waltham, D. (2015), Milankovitch period uncertainties and their impact on
828 cyclostratigraphy, J. Sediment. Res., 85, 990-998, doi:10.2110/jsr.2015.66
829 Wendler, I. (2013), A critical evaluation of carbon isotope stratigraphy and
830 biostratigraphic implications for Late Cretaceous global correlation, Earth
831 Sci. Rev., 126, 116-146, doi:10.1016/j.earscirev.2013.08.003.
832 Wendler, J. E., S. R. Meyers, I. Wendler, and J. Kuss (2014), A million-year-scale
833 astronomical control on Late Cretaceous sea-level. Newsl. Stratigr., 47, 1-
834 19, doi:10.1127/0078-0421/2014/0038.
835 Wu, H., Zhang, S., Jiang, G., Hinnov, L., Yang, T., Li, H., Wan, X., Wang, C. (2013),
836 Astrochronology of the Early Turonian–Early Campanian terrestrial
837 succession in the Songliao Basin, northeastern China and its implications
838 for long-period behavior of the Solar System. Palaeogeogr. Palaeoclimatol.
839 Palaeoecol., 385, 55–70.
840 Zeebe, R.E. (2017), Numerical Solutions for the Orbital Motion of the Solar
841 System over the Past 100 Myr: Limits and New Results, The Astronomical
842 Journal, 154, no. 5, doi: 10.3847/1538-3881/aa8cce
843 Zeebe, R.E., and Lourens, L.J. (2019), Solar System chaos and the Paleocene–
844 Eocene boundary age constrained by geology and astronomy. Science,
845 365 (6456), 926-929, doi:10.1126/science.aax0612.
846 Zeebe, R. E., Westerhold, T., Littler, K., & Zachos, J. C. (2017), Orbital forcing of the
847 Paleocene and Eocene carbon cycle. Paleoceanography, 32, 440–465.
848 https://doi.org/10.1002/2016PA003054
849 Zeeden, C., Meyers, S.R., Lourens, L.J., Hilgen, F.J. (2015), Testing astronomically
850 tuned age models, Paleoceanography, 30, 369-383, doi:
851 10.1002/2014PA002762.

852 **FIGURE CAPTIONS**

853

854 **Table 1.** Comparison of published age estimates for the Early Turonian. CIE =
855 carbon-isotope excursion; n.d. = not defined explicitly.

856

857 **Table 2.** Age calibration of chronostratigraphic boundaries and carbon-isotope
858 excursions (CIE) in reference boreholes.

859

860 **Figure 1.** Overview of chronology (GTS 2012, 2020) and carbon-isotope
861 stratigraphy of the study interval. Major carbon-isotope anomalies (CIEs) are
862 highlighted by blue shading (positive anomalies) and yellow shading (negative
863 anomalies). The Lower/Middle Turonian boundary is defined by the first
864 occurrence (FO) of *Collignoniceras woollgari*, which is penecontemporaneous
865 with the Lulworth CIE (Jarvis et al. 2006). **(a)** English Chalk reference curve;
866 modified after Jarvis et al. (2006); age model after Pearce et al. (2020). **(b)**
867 Borehole Bch-1, Bohemian Cretaceous Basin, interpolated age (Uličný et al. 2014;
868 Jarvis et al. 2015). **(c)** USGS #1 Portland core, Western Interior Basin; lower part
869 (black) after Sageman et al. 2006 ("min option" in their fig. 1); upper part (blue)
870 after Joo and Sageman (2014). **(d)** Wunstorf core, age calibrated (floating
871 astrochronology after Voigt et al. 2008). **(e)** Contessa section plotted in the depth
872 domain (Stoll and Schrag 2000). **(f)** Eccentricity maxima interpreted by
873 Batenburg et al. (2016). Numbers refer to the sequence of cycles in the solution
874 La2011 (Laskar et al. 2011b).

875

876 **Figure 2.** Paleogeographic context. **(a)** Plate tectonic reconstruction after Hay et
877 al. (1999). Land/sea distribution is simplified after the PALEOMAP Project, C.R.
878 Scotese (www.scotese.com). BCB = the Bohemian Cretaceous Basin. **(b)** Detail of
879 the study area (modified after Uličný et al. 2009, 2014) plotted in the present-
880 day coordinate system.
881
882 **Figure 3.** Reference boreholes and data discussed in this study. Numbers 1a
883 through 46 denote correlation markers (see Figs. S1-S6 for a detailed correlation
884 and Figs. S7-S8 for lithology). Carbon isotope excursions in the Lower Turonian
885 are labelled "se-20", "be-20", etc., where "se" and "be" refer to the location
886 (Sedlec and Beřkovice, respectively). Grey shading highlights the Oceanic Anoxic
887 Event II (OAE II). GR = gamma ray, RES = resistivity, XNN = neutron-neutron log.
888 Blue shading marks the correlation uncertainty of the Cenomanian/Turonian
889 and Lower/Middle Turonian boundaries (Figs. S1-S6 and S13). Type A cycles =
890 carbonate-dominated lithofacies; Type B = siliciclastic-dominated lithofacies
891 (Figs. S7 and S8). Lithostratigraphy after Čech et al. (1980). Genetic sequences
892 after Uličný et al. (2009). Wavy line = omission surface.
893
894 **Figure 4**. Spectral estimates, borehole J-719670. **(a)** Resistivity log (RES). Labels
895 1a through 45 denote correlation markers most of which correspond to maxima
896 in the S_4 signal. **(b)** MTM (3 2π) amplitude estimate for the common logarithm of
897 RES obtained with a 7-m moving window (EHA). F-test significance estimates are
898 presented in Fig. S9. Potential signals are labelled S_1 through S_4. Interference
899 patterns (IP) are highlighted by arches ")". Note that the amplitude and F-test
900 maxima corresponding to the S_4 signal migrate towards lower frequencies

paralleling an upward increase in sand contents and a large-scale progradational pattern in the coeval siliciclastic system (Fig. S1). The EHA pattern resembles a reciprocal function of signal wavelength, consistent with a linear increase in sedimentation rate. **(c)** Resistivity log and EHA amplitude after removal of the linear trend. Intervals of constructive interference of S_{4a} and S_{4b} signals (x) delineate ~100-kyr eccentricity maxima. **(d)** MTM and ASM results for the interval 380-418m. The ASM analysis is based on all F-test maxima exceeding the 0.90 level between frequencies 0 and 5 cycle/m. Ho/SL = null-hypothesis significance level. Sedimentation rates constrained by GTS 2020 are shown by ochre shading. Blue lines and symbols indicate the best fit to the astronomical terms of long eccentricity (E_1; 405 kyr period), short eccentricity ($E_{2,3}$; 127 and 97 kyr periods), obliquity ($O_{1,2}$; 49 and 39 kyr periods) and precession (P_{1-4}; 23 - 19 kyr periods; Tab. S2a).

Figure 5. Correlation of astronomical signals. **(a, b)** Astronomical signatures in boreholes J-719670 and J-650704; setup as in Fig. 4. Intervals of constructive interference of the S_{4a} and S_{4b} signals (x) delineate ~100-kyr eccentricity maxima. Series of strong interference patterns (IP) in the EHA plot mark 405-kyr maxima (ochre shading) superimposed upon a maximum in ~2.4-Myr modulation (cf. Fig. 5c). Note that the fidelity of S_4 envelopes and phase of S_1 (405-kyr) signals would remain uncertain without IP (cf. Laurin et al. 2016). **(c)** Comparison with the astronomical solution La2010d (Laskar et al. 2011a); the nearest interval compatible with eccentricity phasing in the study interval. Filter setup (Taner, roll-off rate 4×10^4): J-719670, S_4 = 1.00±0.30 cycle/m, S_2 = 0.20±0.05 cycle/m, S_1 = 0.05±0.01 cycle/m; J-650704, S_4 = 1.15±0.35 cycle/m, S_2

926 = 0.23±0.05 cycle/m, S_1 = 0.05±0.01 cycle/m; La2010d, prec. = 50±15 cycle/Myr,
927 short ecc. = 10±3 cycle/Myr, long ecc. = 2.47±0.5 cycle/Myr.
928
929 **Figure 6.** Interpretation of astronomical signatures, borehole 4523-A. **(a)**
930 Carbon-isotope data, greyscale and filtered signals. Filter setup (Taner, roll-off
931 rate 4×10^4): S_4 = 1.00±0.30 cycle/m, S_2 = 0.23±0.05 cycle/m. **(b)** EHA spectral
932 estimate for greyscale data; dashed lines denote the expected trace of the S_4
933 (precessional) signal inferred from correlation to borehole J-719670 (5-m
934 moving average). **(c)** MTM and ASM estimates for greyscale data, interval 190-
935 203 m. See Tables S2a and S2b for ASM setup. Sedimentation rates constrained
936 by GTS 2020 are shown by ochre shading.
937
938 **Figure 7.** Eccentricity framework constraining the tuning target (see also Figs.
939 S14 and S15). **(a-d)** Filtered precessional and eccentricity signals in reference
940 boreholes. Maxima in short-eccentricity cycles (~100 kyr; labelled ecc1 through
941 ecc11) are inferred using a combination of bandpassed S_2 and amplitude
942 envelopes of the precessional signal (S_4): in the middle and upper parts of the
943 succession that exhibit distinct precessional modulations (Fig. 5), the ~100-kyr
944 maxima are based primarily on amplitude envelopes of the S_4 signal in borehole
945 J-719670; the lower part of the succession exhibits less stable precessional
946 signals; ~100-kyr maxima ecc1-ecc3 are therefore placed at maxima in the S_2
947 bandpass (see text). Long-eccentricity, 405-kyr, maxima (ochre shading) are
948 placed at intervals with strong precessional interference patterns (Figs. 4 and 5).
949 **(e)** Bundling ratios of precessional (P) vs. short-eccentricity (E) signals in the
950 study interval. **(f)** Correlation to the nearest compatible segments of the

951 astronomical solutions La2010d (Laskar et al. 2011a) and La2004 (Laskar et al.
952 2004). Filter setup (Taner, roll-off rate 4×10^4): Bch-1, S_2 = 0.15±0.04 cycle/m;
953 4523-A, S_4 = 1.00±0.30 cycle/m, S_2 = 0.23±0.05 cycle/m, S_1 = 0.05±0.01 cycle/m;
954 J-719670, S_4 = 1.00±0.30 cycle/m, S_2 = 0.20±0.05 cycle/m, S_1 = 0.05±0.01
955 cycle/m; J-650704, S_4 = 1.15±0.35 cycle/m, S_2 = 0.23±0.05 cycle/m, S_1 =
956 0.05±0.01 cycle/m; La2004 and La2010d, prec. = 50±15 cycle/Myr, short ecc. =
957 10±3 cycle/Myr, long ecc. = 2.47±0.5 cycle/Myr.
958
959 **Figure 8.** Updated chronology and eccentricity phasing for the Early Turonian.
960 **(a)** Chronology; duration of the Early Turonian is estimated as 885 ±41 kyr (Tab.
961 2); the floating astrochronology is anchored to the C/T boundary, 93.9 ±0.15 Myr
962 ago (Meyers et al. 2012a). Duration of the Cenomanian part of OAE II (shaded) is
963 based on Sageman et al. (2006) and Ma et al. (2014); Fig. S13. **(b)** The nearest
964 segment of the astronomical solution La2010d (Laskar et al. 2011a) whose
965 eccentricity phasing is compatible with eccentricity signatures in the study
966 interval (Figs. 4, 5 and 7). Filter setup as in Figure 7. **(c)** Timing of 405-kyr
967 eccentricity maxima and minima inferred in this study. Numbers refer to the
968 sequence of cycles in the 405-kyr metronome (Laskar 2020). Comparison with
969 eccentricity phasing at Furlo (Italy) is shown at the bottom; IRM = Isothermal
970 Remanent Magnetization; black = sum of eccentricity components; red = 405 kyr
971 (Laurin et al. 2016). **(d)** EHA estimate for age-calibrated $\delta^{13}C_{org}$, borehole 4523-A.
972 **(e)** Age-calibrated carbon-isotope curves. The Early Turonian interval of 4523-A
973 is calibrated in high-resolution as described in sections 4.4 and 4.5. A linear
974 sedimentation rate of 1.55 cm/kyr is applied to the Cenomanian segment of
975 4523-A, beneath marker 1a (grey part of $\delta^{13}C$ curve; Fig. S13). Age calibration of

Wunstorf after Voigt et al. (2008), and Portland after Sageman et al. 2006 (black) and Joo and Sageman 2014 (grey). The age model for English Chalk (Jarvis et al. 2006; Pearce et al. 2020) has been updated by adjusting the duration of the Early Turonian to 885 kyr; option 1 = Eastbourne and Culver data are interpolated to the GTS2012 age of FO *M.n.* (details in Pearce et al. 2020); option 2 = linear interpolation between C/T boundary and FO *C.w.*, ignoring the GTS age of FO *M.n*. Abbreviations: V08 = Voigt et al. (2008), J14 = Joo and Sageman (2014), B20 = Boulila et al. (2020), *I.c.* = *Inoceramus cuvieri, C.w.* = *Collignoniceras woollgari, M.n.* = *Mammites nodosoides, M.pu.* = *Mytiloides puebloensis, W.d.* = *Watinoceras devonense, M.g.* = *Metoicoceras geslinianum.*

Figure 1.

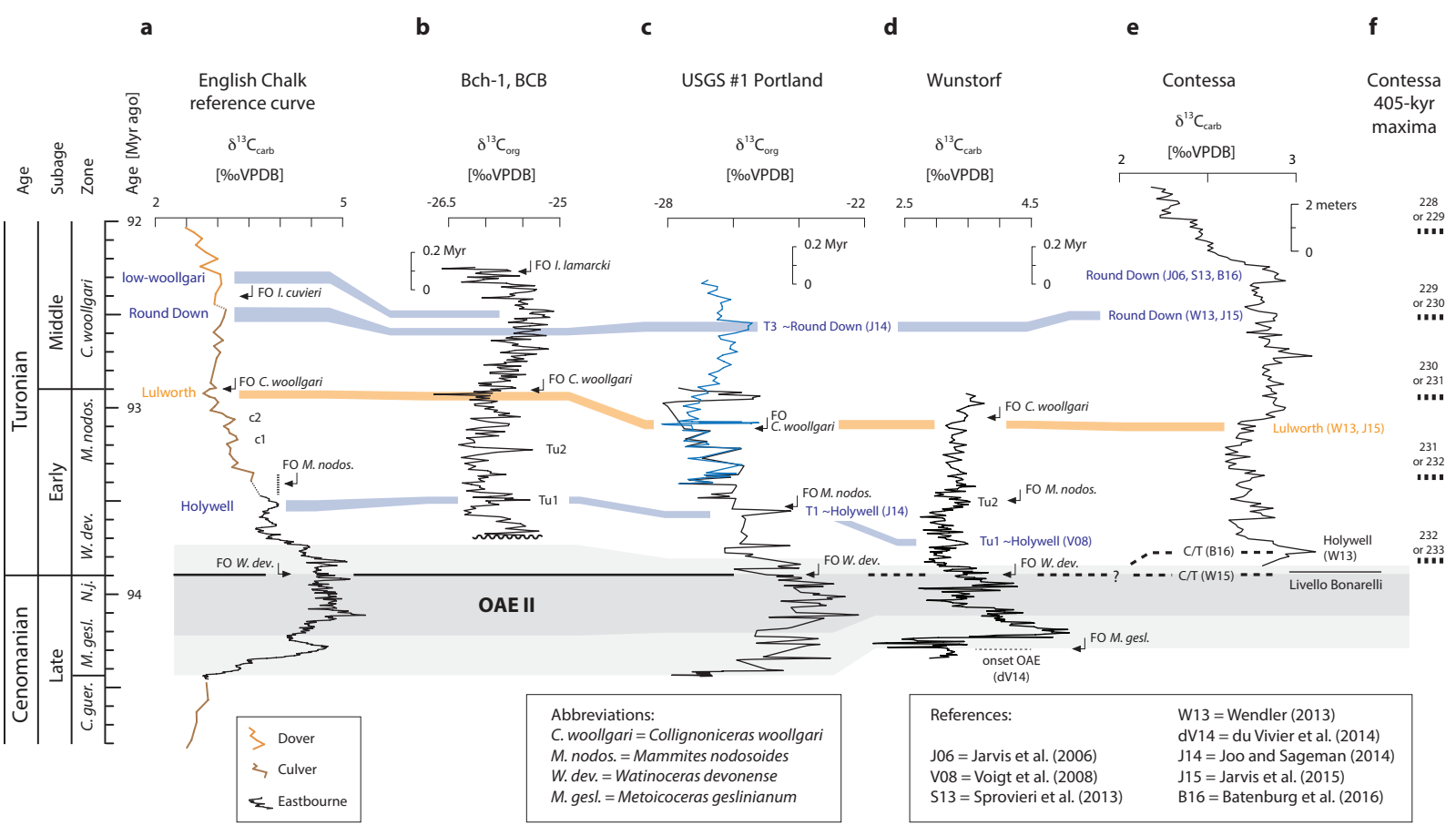
a
b
c
d
e
f
English Chalk reference curve
Bch-1, BCB
USGS #1 Portland
Wunstorf
Contessa
Contessa 405-kyr maxima
Age
Subage
Zone
Age [Myr ago]
δ13Ccarb [‰VPDB]
δ13Corg [‰VPDB]
Turonian
Cenomanian
Middle
Early
Late
C. woollgari
M. nodos.
W. dev.
N.j.
M. gesl.
C. guer.
low-woollgari
Round Down
Lulworth
Holywell
FO I. cuvieri
FO I. lamarcki
FO C. woollgari
FO M. nodos.
FO W. dev.
FO M. gesl.
c2
c1
Tu2
Tu1
T3 ~Round Down (J14)
T1 ~Holywell (J14)
Tu1 ~Holywell (V08)
Round Down (J06, S13, B16)
Round Down (W13, J15)
Lulworth (W13, J15)
Holywell (W13)
C/T (B16)
C/T (W15)
Livello Bonarelli
OAE II
onset OAE (dV14)
0.2 Myr
2 meters
228 or 229
229 or 230
230 or 231
231 or 232
232 or 233
Dover
Culver
Eastbourne
Abbreviations:
C. woollgari = Collignoniceras woollgari
M. nodos. = Mammites nodosoides
W. dev. = Watinoceras devonense
M. gesl. = Metoicoceras geslinianum
References:
J06 = Jarvis et al. (2006)
V08 = Voigt et al. (2008)
S13 = Sprovieri et al. (2013)
W13 = Wendler (2013)
dV14 = du Vivier et al. (2014)
J14 = Joo and Sageman (2014)
J15 = Jarvis et al. (2015)
B16 = Batenburg et al. (2016)

Figure 2.

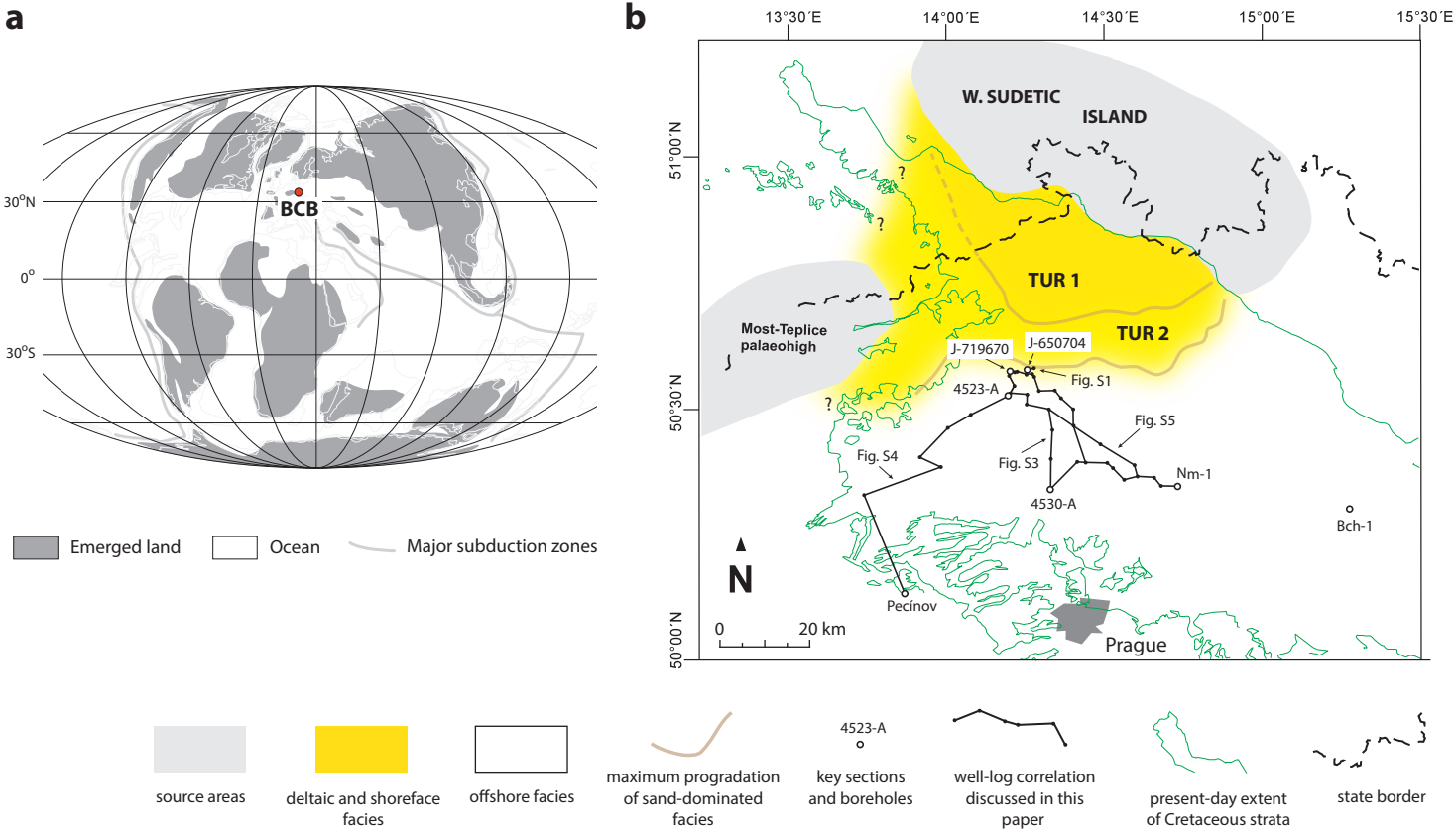
a
30°N
0°
30°S
BCB
Emerged land
Ocean
Major subduction zones
b
13°30´E
14°00´E
14°30´E
15°00´E
15°30´E
51°00´N
50°30´N
50°00´N
W. SUDETIC
ISLAND
TUR 1
TUR 2
Most-Teplice
palaeohigh
J-719670
J-650704
Fig. S1
4523-A
Fig. S5
Fig. S4
Fig. S3
Nm-1
4530-A
Bch-1
N
0
20 km
Pecínov
Prague
source areas
deltaic and shoreface facies
offshore facies
maximum progradation of sand-dominated facies
4523-A
key sections and boreholes
well-log correlation discussed in this paper
present-day extent of Cretaceous strata
state border

Figure 3.

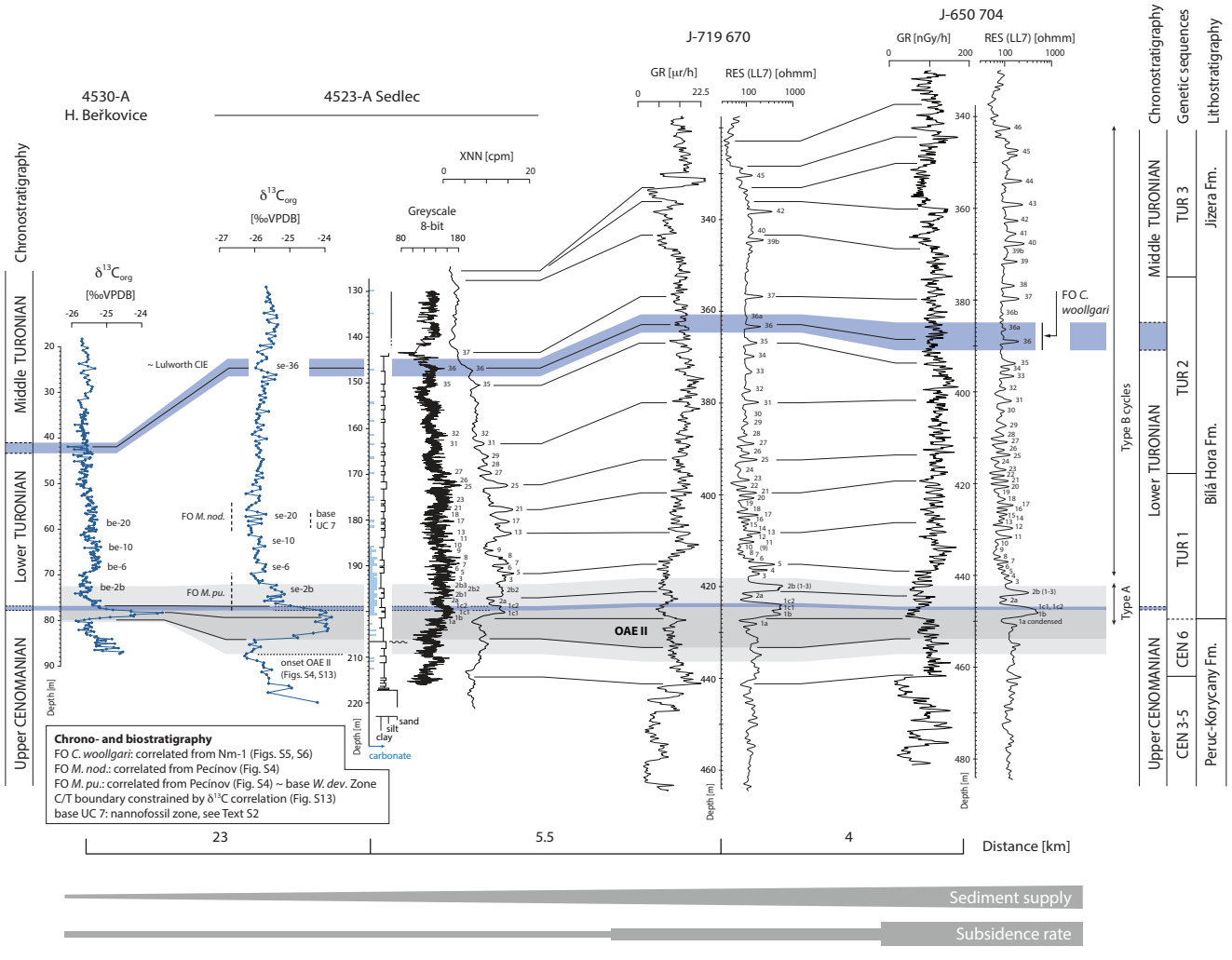
4530-A
H. Beřkovice
4523-A Sedlec
J-719 670
J-650 704
GR [µr/h]
RES (LL7) [ohmm]
GR [nGy/h]
RES (LL7) [ohmm]
XNN [cpm]
Greyscale 8-bit
δ13Corg [‰VPDB]
~ Lulworth CIE
FO M. nod.
FO M. pu.
base UC 7
onset OAE II (Figs. S4, S13)
OAE II
FO C. woollgari
Type B cycles
Type A
sand
silt
clay
carbonate
Depth [m]
Distance [km]
23
5.5
4
Chronostratigraphy
Genetic sequences
Lithostratigraphy
Middle TURONIAN
Lower TURONIAN
Upper CENOMANIAN
TUR 3
TUR 2
TUR 1
CEN 6
CEN 3-5
Jizera Fm.
Bílá Hora Fm.
Peruc-Korycany Fm.
Chrono- and biostratigraphy
FO C. woollgari: correlated from Nm-1 (Figs. S5, S6)
FO M. nod.: correlated from Pecínov (Fig. S4)
FO M. pu.: correlated from Pecínov (Fig. S4) ~ base W. dev. Zone
C/T boundary constrained by δ13C correlation (Fig. S13)
base UC 7: nannofossil zone, see Text S2
Sediment supply
Subsidence rate

Figure 4.

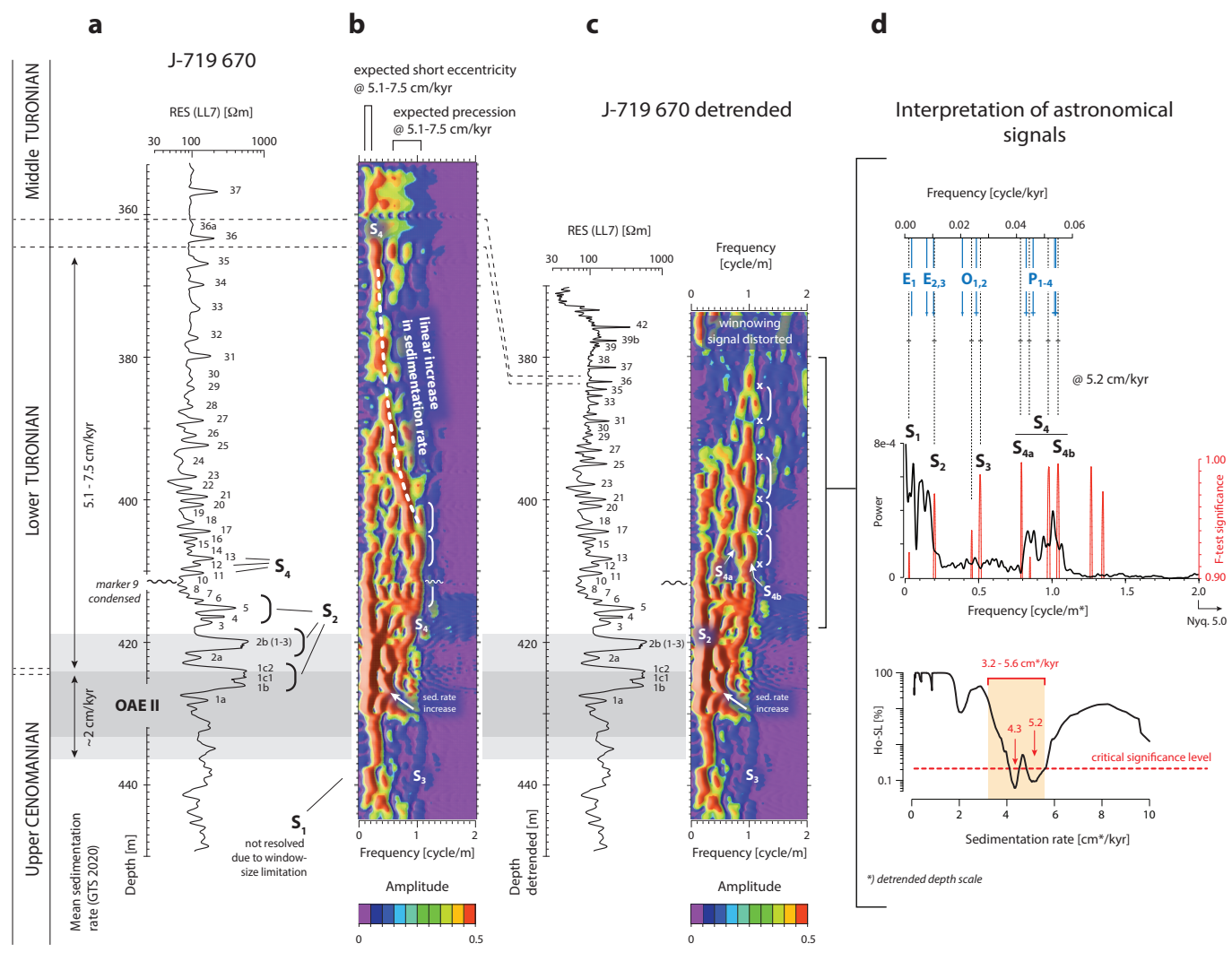
a
J-719 670
RES (LL7) [Ωm]
30
100
1000
Middle TURONIAN
Lower TURONIAN
Upper CENOMANIAN
5.1 - 7.5 cm/kyr
~2 cm/kyr
OAE II
marker 9
condensed
S4
S2
S1
not resolved
due to window-
size limitation
Depth [m]
Mean sedimentation
rate (GTS 2020)
b
expected short eccentricity
@ 5.1-7.5 cm/kyr
expected precession
@ 5.1-7.5 cm/kyr
linear increase
in sedimentation rate
sed. rate
increase
Frequency [cycle/m]
Amplitude
c
J-719 670 detrended
RES (LL7) [Ωm]
Frequency
[cycle/m]
winnowing
signal distorted
Depth
detrended [m]
d
Interpretation of astronomical
signals
Frequency [cycle/kyr]
E1
E2,3
O1,2
P1-4
@ 5.2 cm/kyr
Power
F-test significance
Frequency [cycle/m*]
Nyq. 5.0
3.2 - 5.6 cm*/kyr
Ho-SL [%]
4.3
5.2
critical significance level
Sedimentation rate [cm*/kyr]
*) detrended depth scale

Figure 5.

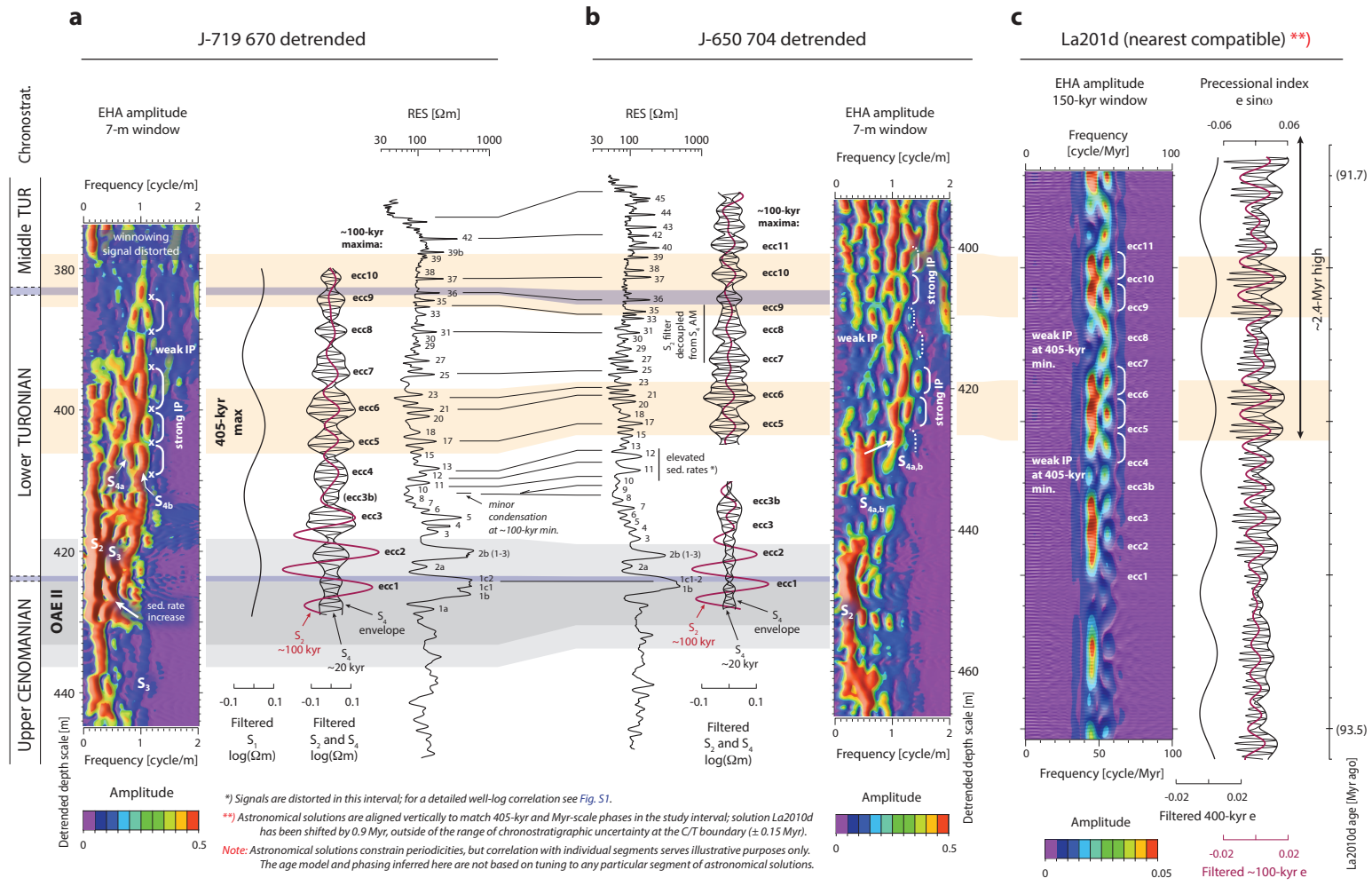

*) Signals are distorted in this interval; for a detailed well-log correlation see Fig. S1.

**) Astronomical solutions are aligned vertically to match 405-kyr and Myr-scale phases in the study interval; solution La2010d has been shifted by 0.9 Myr, outside of the range of chronostratigraphic uncertainty at the C/T boundary (± 0.15 Myr).

Note: Astronomical solutions constrain periodicities, but correlation with individual segments serves illustrative purposes only. The age model and phasing inferred here are not based on tuning to any particular segment of astronomical solutions.

Figure 6.

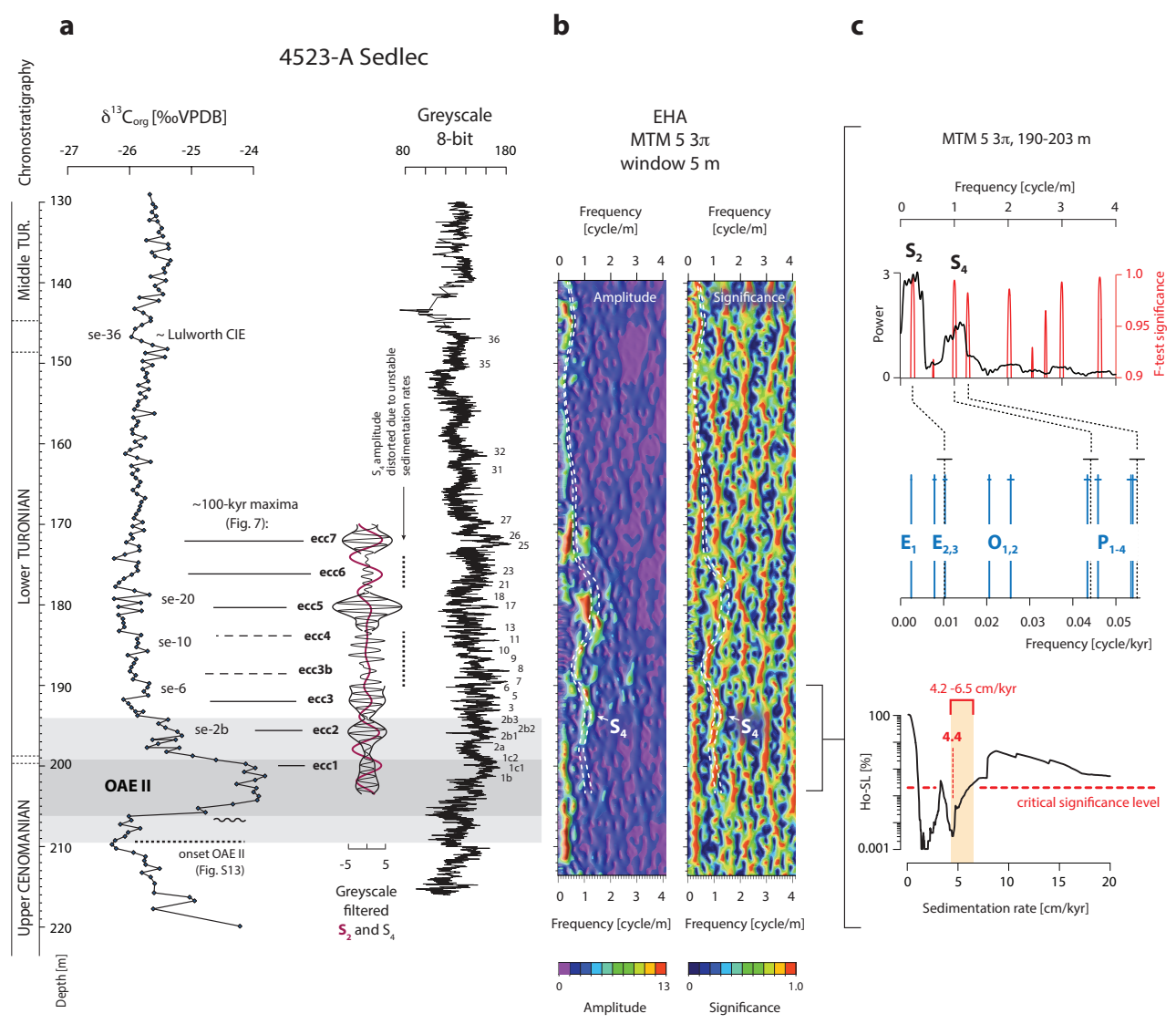
a
4523-A Sedlec
Chronostratigraphy
δ13Corg [‰VPDB]
-27
-26
-25
-24
Greyscale
8-bit
80
180
Middle TUR.
Lower TURONIAN
Upper CENOMANIAN
130
140
150
160
170
180
190
200
210
220
Depth [m]
se-36
~ Lulworth CIE
~100-kyr maxima
(Fig. 7):
ecc7
ecc6
se-20
ecc5
se-10
ecc4
ecc3b
se-6
ecc3
se-2b
ecc2
ecc1
OAE II
onset OAE II
(Fig. S13)
S4 amplitude
distorted due to unstable
sedimentation rates
-5
5
Greyscale
filtered
S2 and S4
b
EHA
MTM 5 3π
window 5 m
Frequency
[cycle/m]
0
1
2
3
4
Amplitude
Significance
S4
Frequency [cycle/m]
0
13
Amplitude
0
1.0
Significance
c
MTM 5 3π, 190-203 m
Frequency [cycle/m]
S2
S4
Power
3
0
1.0
0.95
0.9
F-test significance
E1
E2,3
O1,2
P1-4
0.00
0.01
0.02
0.03
0.04
0.05
Frequency [cycle/kyr]
4.2 -6.5 cm/kyr
100
4.4
Ho-SL [%]
critical significance level
0.001
0
5
10
15
20
Sedimentation rate [cm/kyr]

Figure 7.

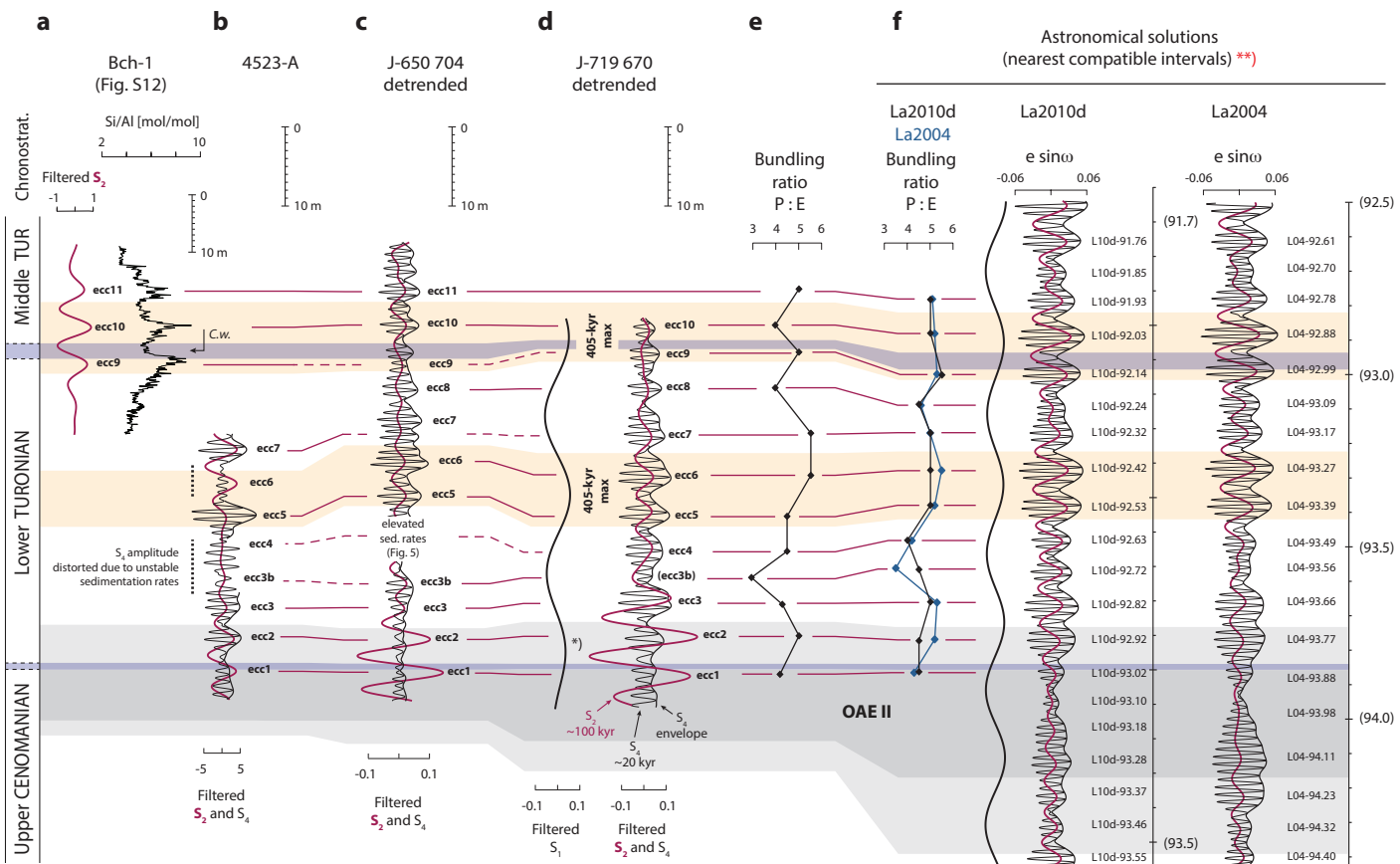

*) *Filtered S_2 is biased due to condensation at ecc3b (Fig. 4) and lithological change (Type A vs. Type B transition; Fig. S7); placing the 405-kyr maximum between ecc2 and ecc3, i.e., approximately one short-eccentricity cycle above the maximum in filtered S_1 preserves the 1:4 bundling of long- vs. short-eccentricity cycles.*

**) *Astronomical solutions are aligned vertically to match 405-kyr and Myr-scale phases in the study interval; solution La2010d has been shifted 0.9 Myr towards the younger end of the time scale, outside of the range of chronostratigraphic uncertainty at the C/T boundary (± 0.15 Myr).*

Note: Astronomical solutions constrain periodicities of astronomical terms, but correlation with individual segments serves illustrative purposes only. The age model and eccentricity phasing inferred here are not based on tuning to any particular segment of astronomical solutions (see text).

Figure 8.

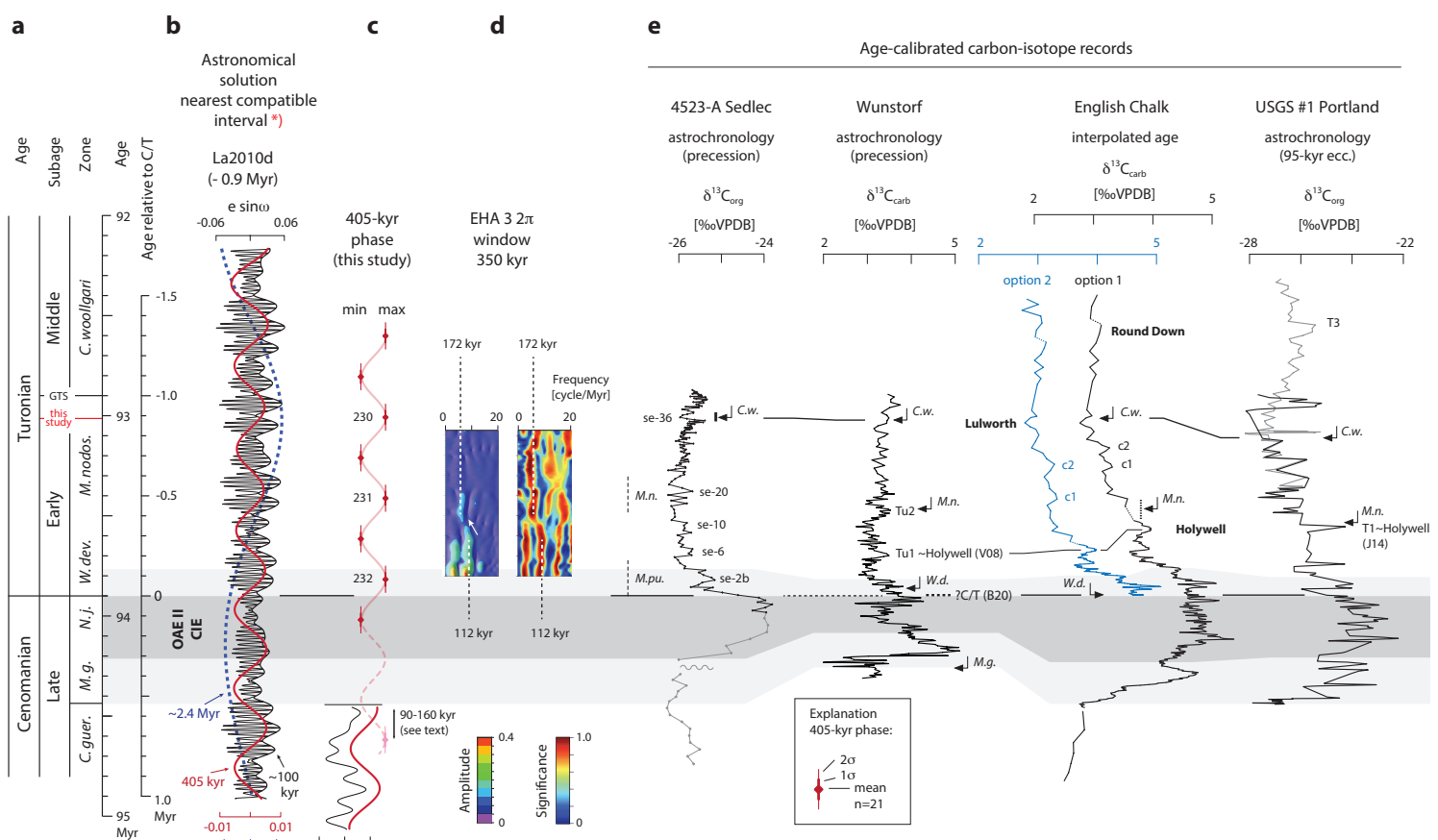

*) *The nearest segment of La2010d compatible with eccentricity phasing in the study interval (Figs. 5 and 7); to find the nearest fit, the La2010d curve has been shifted 0.9 Myr towards the younger end of the time scale, outside of the range of chronostratigraphic uncertainty (± 0.15 Myr).*

Note: Astronomical solutions constrain periodicities of astronomical terms, but correlation with individual segments serves illustrative purposes only. The age model and eccentricity phasing inferred here are not based on tuning to any particular segment of astronomical solutions (see text).

Reference	Location	Duration of Early Turonian [Myr]	Un-certainty [± Myr]	Pros	Cons
Sageman et al. (2006); Meyers et al. (2012a)	Portland	0.785	n.d.	Robust astronomical signature	Short-eccentricity tuning target, monochromatic (95 kyr); modulation of the tuning target not considered
Voigt et al. (2008)	Wunstorf	0.84	n.d.	Precession-scale resolution; robust astronomical signature	Precession-paced chronology does not reach the top of Early Turonian; modulation of the tuning target not considered
GTS 2012 Ogg and Hinnov (2012)		1.0	n.d.		Meyers et al. (2012a) misquoted [1]); Voigt et al. (2008) not considered
Sprovieri et al. (2013)	Bottaccione	0.6-0.8	n.d.	Well-defined 405-kyr signature	No macrofossil zonation; reduced resolution near C/T boundary
Eldrett et al. (2015; their fig. 11)	Iona	1.14	n.d.	High-resolution astronomical signature	No macrofossil zonation; Early/Middle Turonian boundary controversial, placed into a major positive CIE
Batenburg et al. (2016)	Contessa	0.6-1.2	n.d.	Well-defined eccentricity signature	No macrofossil zonation; C/T boundary controversial (cf. Wendler 2013; Fig. 1)
GTS 2020 Gale et al. (2020)		1.0	n.d.		Adopted from GTS 2012 (see above)
This study	Bohemian Cretaceous Basin	0.885	0.041	Precession-scale resolution; robust eccentricity phasing; modulation of the tuning target included	Macrofossil zones correlated from adjacent boreholes (correlation uncertainty acknowledged in the uncertainty range)

[1]) The duration of W. devonense Zone is given as 0.35 Myr with reference to Meyers et al. (2012a); Meyers et al. (2012a), however, indicate ~0.2 Myr (two short-eccentricity cycles; their figure 1).

Table 1. Comparison of published age estimates for the Early Turonian. CIE = carbon-isotope excursion; n.d. = not defined explicitly.

Stratigraphic level	J-719670			J-650704			4523-A			J-719670 anchored to C/T	
	Depth [m]	Floating age (median) [kyr]	Uncert. 95% CI [kyr]	Depth [m]	Floating age (median) [kyr]	Uncert. 95% CI [kyr]	Depth [m]	Floating age (median) [kyr]	Uncert. 95% CI [kyr]	Option 1 [2]) [Myr ago]	Option 2 [3]) [Myr ago]
Base Middle Tur. (FO *C.w.*), upper limit	360.7	**-902**	+16/-20	384.9	-903	+14/-14	144.50	-915	+29/-22	93.00 ±0.16	93.05 ±0.06
Lulworth CIE ($\delta^{13}C_{org}$ trough)							146.75	-890	+22/-27		
Base Middle Tur. (FO *C.w.*), lower limit	364.5	**-865**	+22/-19	391.0	-860	+22/-19	148.50	-872	+23/-21	93.04 ±0.16	93.09 ±0.06
CIE "se-20" peak							178.75	-521	+19/-21		
CIE "se-10" peak							185.75	-315	+18/-20		
CIE "se-6" peak							191.25	-203	+12/-15		
CIE "se-2b" peak							196.25	-79	+15/-16		
C/T boundary, upper limit	423.6	-11	+7/-17	446.8	-11	+7/-22	198.75	-17	+9/-16	93.90 ±0.15	93.95 ±0.05
C/T boundary, lower limit	424.5	13	+4/-3	447.5	15	+3/-3	199.75	9	+2/-3		
Onset of OAE II recovery							199.75	9	+2/-3		
Duration of Early Turonian		**885**	**±41 [1])**		884	±43 [1])		890	±48 [1])		

[1]) Combined uncertainty, 95% CI, assuming uniform distribution between lower and upper limits of chronostratigraphic boundaries and normal distribution of floating ages
[2]) C/T boundary dated as 93.90 ±0.15 Myr ago (Meyers et al. 2012a); combined uncertainty (summation in quadrature), 95% CI
[3]) C/T boundary dated as 93.95 ±0.05 Myr ago (Jones et al. 2020); combined uncertainty (summation in quadrature), 95% CI
C.w. = *Collignoniceras woollgari*
CI = confidence interval

Table 2. Age calibration of chronostratigraphic boundaries and carbon-isotope excursions (CIE) in reference boreholes.